

MESSENGER observations of flow braking and flux pileup of dipolarizations in Mercury's magnetotail: Evidence for current wedge formation

Ryan M. Dewey^{1*}, James A. Slavin¹, Jim M. Raines¹, Abigail R. Azari¹, Weijie Sun¹

¹Department of Climate and Space Sciences and Engineering, University of Michigan, Ann Arbor, MI, USA.

*Corresponding author: rm Dewey@umich.edu

Key points:

- Dipolarizations in Mercury's magnetotail encounter strong magnetic pressure gradients near the planet that brake their fast sunward flow
- Only a small fraction of dipolarizations reach the nightside surface; most brake and contribute to magnetic flux pileup
- Pileup results from the interaction of multiple dipolarizations and is consistent with Earth-like substorm current wedge formation

Abstract

Similar to Earth, Mercury's magnetotail experiences frequent dipolarization of the magnetic field. These rapid (~ 2 s) increases in the northward component of the tail field ($\Delta B_z \sim 30$ nT) at Mercury are associated with fast sunward flows (~ 200 km/s) that enhance local magnetic field convection. Differences between the two magnetospheres, namely Mercury's smaller spatiotemporal scales and lack of an ionosphere, influence the dynamics of dipolarizations in these magnetotails. At Earth, the braking of fast dipolarization flows near the inner magnetosphere accumulates magnetic flux and develops the substorm current wedge. At Mercury, flow braking and flux pileup remain open topics. In this work, we develop an automated algorithm to identify dipolarizations, which allows for statistical examination of flow braking and flux pileup in Mercury's magnetotail. We find that near the inner edge of the plasma sheet, steep magnetic pressure gradients cause substantial braking of fast dipolarization flows. The dipolarization frequency and sunward flow speed decrease significantly within a region ~ 500 km thick located at ~ 900 km altitude above Mercury's local midnight surface. Due to the close proximity of the braking region to the planet, we estimate ~ 10 - 20% of dipolarizations may reach the nightside surface of the planet. The remaining dipolarizations exhibit prolonged statistical flux pileup within the braking region similar to large-scale dipolarization of Earth's inner magnetosphere. The existence of flow braking and flux pileup at Mercury indicates a current wedge may form, although the limitations imposed by Mercury's magnetosphere require the braking of multiple, continuous dipolarizations for current wedge formation.

1. Introduction

Dipolarizations are common to the magnetotails of both Earth and Mercury. A product of intense nightside reconnection, dipolarizations represent newly-closed, more dipolar field lines that are carried planetward by fast reconnection outflows (e.g., Sitnov et al., 2009; Runov et al., 2012; Fu et al., 2013). Observed in situ, dipolarizations are identified by the sharp, step-like increase in the northward component of the magnetic field (known as the dipolarization front; e.g., Nakai et al., 2002) that precedes the newly reconnected flux tube (known as the dipolarizing flux bundle; Liu et al., 2013). Since dipolarizations are a result of reconnection between the low-density magnetotail lobes, they tend to be depleted in thermal plasma and embedded within fast sunward flows (e.g., Angelopoulos et al., 1992; Sergeev et al., 1996; Runov et al., 2015). Additional signatures of dipolarizations include an

50 enhanced cross-tail electric field, enhanced thermal plasma temperature, and enhanced energetic particle
51 flux compared to the surrounding plasma sheet (e.g., Runov et al., 2009; Runov et al. 2013).

52
53 At Earth, dipolarizations contribute major roles in mass and magnetic flux transport, particle
54 acceleration, and substorm current wedge formation. Although individual dipolarizations are localized in
55 their cross-tail extent ($\sim 1-3 R_E$, where R_E is Earth's mean radius, 6,371 km), their faster sunward flow,
56 stronger northward magnetic field, and enhanced cross-tail electric field compared to the surrounding
57 plasma sheet result in dipolarizations transporting the majority of magnetic flux from the mid-tail to the
58 near-tail, particularly during geomagnetically active intervals (Liu et al., 2014). As a dipolarization
59 travels planetward, particles interacting with its magnetic structure, particularly those trapped by the
60 local magnetic field gradients about the dipolarization front, can experience betatron and Fermi
61 acceleration (e.g., Ashour-Abdalla et al., 2011; Birn et al., 2013; Gabrielse et al., 2016; Ukhorskiy et al.,
62 2018). Only a small fraction of dipolarizations penetrate into the inner magnetosphere, with the majority
63 of dipolarizations stopping near the inner edge of the plasma sheet (Shiokawa et al., 1997, Dubyagin et
64 al., 2011; Ohtani et al., 2006). Near this boundary, dipolarizations brake due to steep magnetic pressure
65 gradients, and their magnetic flux accumulates (or piles up) (Birn et al., 2011; Karlsson et al., 2015). As
66 additional dipolarizations brake and accumulate, this flux pileup region can expand both azimuthally and
67 downtail, resulting in a large-scale dipolarization of the near-tail region (e.g., Baumjohann et al., 1999;
68 Birn et al., 2011; Birn et al., 2019; Merkin et al., 2019). The flux pileup structure is supported by the
69 substorm current wedge, which diverts the cross-tail current into the ionosphere via field-aligned
70 currents of the Region 1-sense (e.g., McPherron et al., 1973; Birn et al., 1999; Kepko et al., 2015a).
71 While the exact mechanics by which dipolarizations (both small- and large-scale) establish and maintain
72 the substorm current wedge, it has been the subject of considerable interest and debate. A contemporary
73 understanding is the "wedgelet" conceptual model in which the individual field-aligned current systems
74 of many small-scale dipolarizations manifest into the substorm current wedge as the dipolarizations
75 brake near the inner magnetosphere (e.g., Liu et al., 2013; Sun et al., 2013; Birn et al., 2019). In this
76 understanding, the current wedge is not a single, monolithic current loop, but that its trending structure
77 emerges from the complex interaction between individual dipolarization current systems.

78
79 Mercury possesses a terrestrial-like magnetosphere, but it operates at substantially smaller
80 spatiotemporal scales, experiences stronger effects from magnetic reconnection, and couples to a
81 different type of inner magnetospheric boundary than Earth's magnetosphere. Mercury's magnetosphere
82 contains many of the same regions as Earth's, including a closed dayside region and an extended
83 magnetotail (see Korth et al., 2018 and Slavin et al., 2018 for comprehensive reviews). Mercury's
84 planetary magnetic field, however, is only $\sim 1\%$ the strength of Earth's (e.g., Anderson et al., 2011),
85 which when combined with the stronger upstream solar wind dynamic pressure at Mercury's orbital
86 location, results in a magnetosphere substantially smaller in both absolute and relative scales. For
87 example, Mercury's subsolar magnetopause stands at $\sim 0.5 R_M \approx 1,200$ km altitude above the planet's
88 dayside surface (Winslow et al., 2013), where R_M is Mercury's mean radius (2,440 km). By contrast,
89 Earth's subsolar magnetopause stands at $\sim 10 R_E \approx 64,000$ km altitude (e.g., Shue et al., 1998).
90 Furthermore, the cross-tail extent of Mercury's magnetotail is $\sim 4 R_M \approx 10,000$ km compared to Earth's
91 of $\sim 40 R_E \approx 255,000$ km (Slavin et al., 2012; Rong et al., 2018; Kaymaz et al., 1992). Consequences of
92 the small dimensions of Mercury's magnetosphere include increased finite gyroradius effects
93 (particularly for heavy ions of planetary origin), increased loss due to surface precipitation, and an
94 increased fraction of the magnetosphere occupied by the planet (e.g., Ogilvie et al., 1997; Delcourt et al.,
95 2003; Delcourt, 2013; Raines et al., 2014). Mercury's hypothetical plasmopause, for example, would be
96 located below the planet's surface due to the planet occupying a large fraction of the magnetosphere and
97 the planet's slow ~ 59 -day rotation. Mercury's magnetosphere also experiences stronger effects from
98 magnetic reconnection. The lower solar wind Alfvén Mach number at Mercury's orbital location results

99 in the formation of thick plasma depletion layers within Mercury's magnetosheath adjacent to the
100 magnetopause (Gershman et al., 2013). These depletion layers allow for more frequent and stronger
101 subsolar magnetopause reconnection that is less sensitive to the direction of the interplanetary magnetic
102 field than at Earth (DiBraccio et al., 2013). Dayside reconnection powers Mercury's ~3 min Dungey
103 cycle and many of the observed dynamics within the magnetosphere (e.g., Slavin et al., 2009; Slavin et
104 al., 2010; Imber & Slavin, 2017; Slavin et al., 2018). Finally, Mercury's large conducting core plays a
105 unique role in magnetospheric dynamics by acting as the magnetosphere's innermost boundary. Mercury
106 lacks an ionosphere so it is expected that its large core (~2,000 km in radius) provides current-closure
107 for static and/or large-scale field-aligned current systems (e.g., Jahunen & Kallio, 2004; Anderson et al.,
108 2014). These current systems pass radially through the thin (~400 km) layer of resistive regolith to
109 connect over the surface of the conducting core. Mercury's core also influences the magnetosphere's
110 interaction with the solar wind. Changes in the solar wind dynamic pressure induce currents on the
111 core's surface that modify the planet's magnetic moment to resist these changes (e.g., Slavin et al.,
112 2014; Jia et al., 2015; Johnson et al., 2016; Jia et al., 2019). Although similar responsive currents may
113 also be induced on the surface of Earth's core, these currents are substantially stronger at Mercury due to
114 Mercury's relatively larger core and the core's close proximity to the magnetopause.
115

116 Given the similar topology between Mercury and Earth's magnetospheres and the dominance of
117 magnetic reconnection in Mercury's dynamics, it is not surprising that dipolarizations are common in
118 Mercury's magnetotail. Similar to those identified at Earth, dipolarizations at Mercury are characterized
119 by a rapid (~2 s) increase in the northward component of the magnetic field (~30 nT) that persists for a
120 short time (~10 s) (Sundberg et al., 2012). Observations from the MESSENGER spacecraft have
121 associated dipolarizations in Mercury's magnetotail with thermal plasma depletion and heating, fast
122 sunward flows, and energetic electron acceleration and injection (Dewey et al., 2017; Dewey et al.,
123 2018; Sun et al., 2018). While Mercury's dipolarizations share many similar features to those at Earth,
124 they also display curious differences. Dipolarizations, for example, are more frequent to Mercury's post-
125 midnight magnetotail, opposite to that of Earth (Sun et al., 2016). Studies of dipolarizations at Mercury
126 have made considerable progress in understanding the signatures and characteristics of these events, yet
127 the dynamics and consequences of Mercury's dipolarizations remain less well understood. One such
128 topic is that of flow braking. Mercury's near-planet reconnection site, located at or planetward of X_{MSM}
129 = $-3 R_M$, is only ~5,000 km above the planet's nightside surface (e.g., Slavin et al., 2009; DiBraccio et
130 al., 2015; Poh et al., 2017a; Smith et al., 2017). Even smaller yet is the distance between the inner edge
131 of Mercury's current sheet and the planet's surface (~500-750 km) (Poh et al., 2017a). Over these
132 distances, the magnetic field increases by a factor of only ~10-100, due to Mercury's weak planetary
133 magnetic field and the large volume of the magnetosphere that the planet occupies. By contrast, the
134 magnetic field at Earth's surface is ~10,000 times greater than in the magnetotail. Is Mercury's magnetic
135 field strong enough to brake dipolarizations and their fast flows? Or do dipolarizations stream directly
136 into the planet's nightside surface unencumbered by the relatively weak magnetic gradients? The
137 answers to these questions carry significance for mass and magnetic flux transport, but are also
138 interdisciplinary, with consequences for exospheric generation and space weathering.
139

140 Initial investigations suggest that braking is likely to occur although the mechanism and location of
141 braking are poorly constrained. Sun et al. (2015) provided the first evidence for flow braking in
142 Mercury's magnetotail by analyzing case studies of Alfvén and compressional waves associated with
143 dipolarizations near the planet, interpreting them to be similar to the waves generated by the braking of
144 flows in Earth's magnetotail (e.g., Panov et al., 2014). At that time, however, the association of
145 Mercury's dipolarizations with fast sunward flows was only speculated. Dewey et al. (2018) established
146 the connection between fast flows and dipolarizations at Mercury by developing a technique to
147 determine average flows by combining together plasma observations of many individual dipolarizations.

148 On the basis of pressure balance, Dewey et al. (2018) hypothesized that these fast flows would break at
149 or planetward of $X_{\text{MSM}'} = -1.3 R_M$, near the expected inner edge of the current sheet (e.g., Poh et al.,
150 2017a). Due to the limited sample size of dipolarizations, however, Dewey et al. (2018) was unable to
151 examine the behavior of flows as a function of location in Mercury's magnetotail and could not support
152 their hypothesis of braking directly. Finally, Poh et al. (2017b) investigated a signature suggestive of
153 magnetic flux pileup within Mercury's midnight current sheet. Poh et al. (2017b) selected current sheet
154 crossings on their ability to be fit by a one-dimensional Harris current sheet and noticed an enhancement
155 of B_z local to midnight between $-1.4 < X_{\text{MSM}'} < -1.7 R_M$. The authors interpreted the B_z enhancement as
156 being due to a current wedge similar to Earth's, however, their work does not connect such a signature
157 to dipolarizations, fast flows, or substorm dynamics. These studies have provided valuable foundational
158 observations and discussions into the topics of flow braking and flux pileup in Mercury's magnetotail
159 but leave the topic largely unconstrained.

161 In this study, we expand upon previous observations and discussions of flow braking and flux pileup in
162 Mercury's magnetotail. We develop an automated algorithm to identify dipolarizations in the magnetic
163 field time series to expand the sample size of events to over an order of magnitude previously examined.
164 This large sample size allows us to employ statistical techniques and form a statistical description of
165 flow braking in lieu of multi-point spacecraft observations. We find that the majority (~80-90%) of
166 dipolarizations brake within a thin (~500 km) region located close to Mercury's surface (~900 km
167 altitude) due to magnetic pressure gradients from the planet's dipole magnetic field. As these flows
168 brake, we observe statistically that their magnetic flux accumulates to form a pileup region that may be
169 associated with an Earth-like current wedge. In Section 2, we describe our data sources and briefly
170 introduce the dipolarization identification algorithm (described in detail in Appendix A). In Section 3,
171 we present both statistical and case study analysis of flow braking and flux pileup, followed by a
172 discussion of these results and the possibility of current wedge formation at Mercury in Section 4. We
173 conclude this investigation in Section 5 with avenues for further research.

175 2. Methodology and data sources

177 For this investigation, we rely on observations from MESSENGER's Magnetometer (MAG; Anderson
178 et al., 2007) and Fast Imaging Plasma Spectrometer (FIPS; Andrews et al., 2007). The MAG instrument
179 measures the local vector magnetic field at 50 ms time resolution. The FIPS sensor measures thermal
180 and low-energy ions with energy-per-charge (e/q) spanning 50 eV/e to 13 keV/e and mass-per-charge
181 (m/q) spanning 1 amu/e to 40 amu/e. FIPS completes a nominal sweep of its energy steps in 10 s. While
182 FIPS has a large instantaneous field of view (~ 1.1π sr), it is unable to measure bulk plasma flows at its
183 native resolution since the spacecraft is three-axis stabilized. To estimate flows, we rely on a statistical
184 reconstruction technique developed by Dewey et al. (2018). This technique assumes plasma flows are
185 subsonic, and utilizes variable field of view pointing across many FIPS scans to construct a more
186 complete velocity space distribution from which bulk plasma flows and their uncertainty can be
187 determined. We refer readers to Dewey et al. (2018) for a technical description and example of this
188 procedure. In Appendix B, we provide a summary of the flow-determination procedure and discuss its
189 application to partial velocity space distributions. We display all MESSENGER observations in the
190 aberrated Mercury solar magnetospheric (MSM') coordinate system, which is centered at Mercury's
191 dipole center with $X_{\text{MSM}'}$ pointing anti-parallel to the solar wind (a radial solar wind speed of 400 km/s
192 is assumed), $Z_{\text{MSM}'}$ pointing northward, and $Y_{\text{MSM}'}$ completing the right-handed system.

194 To identify dipolarizations, we rely exclusively on the MAG observations. While several dipolarization
195 signatures are related to the thermal plasma, a complete FIPS scan has time resolution comparable to the
196 typical duration of a dipolarization (Dewey et al., 2017) and therefore cannot resolve these signatures for

197 all dipolarizations. MAG observations, in contrast, are able to resolve the magnetic field structure of the
198 dipolarization at native resolution. Of the magnetic field signatures of a dipolarization, the sharp, step-
199 like increase in B_z of the dipolarization front is the easiest to detect (e.g., Liu et al. 2013; Sun et al.,
200 2016). We develop an automated algorithm to identify dipolarization fronts in the B_z time series. The
201 algorithm, described in detail in Appendix A, evaluates each point in the time series for a strong,
202 positive, coherent, local gradient in B_z and applies a series of physical tests to determine if such a slope
203 is representative of a dipolarization front or not.

204
205 We apply our dipolarization selection procedure to 1,946 magnetotail intervals that satisfy several
206 criteria. First, to ensure that we are examining the plasma sheet rather than the adjacent magnetotail
207 lobes, we require the 1-minute running average $B_z/|B| > 0.5$ and $\beta > 0.1$, where β is the proton plasma
208 beta. These criteria estimate that the spacecraft samples the closed, mass-loaded magnetic field lines
209 characteristic of the plasma sheet. Other studies of Mercury's magnetotail have used β to identify plasma
210 sheet intervals (e.g., Sun et al., 2017; Poh et al., 2018), but they typically use a higher β threshold. We
211 use a lower threshold since FIPS may underestimate the local plasma beta in the presence of the fast
212 flows associated with dipolarizations (e.g., Dewey et al., 2018) due to the sensor's limited field of view.
213 Second, we exclude intervals contaminated by solar energetic particle events. Third, we limit our survey
214 to the spatial region $-2.5 < X_{\text{MSM}} < 0$, $|Y_{\text{MSM}}| < 1.5$, and $|Z_{\text{MSM}}| < 0.2 R_M$. Finally, to prevent biasing
215 from short intervals, we require that the criteria above must be met for longer than three minutes (the
216 nominal Dungey cycle duration). Together, these 1,946 magnetotail intervals represent an accumulated
217 14,022 minutes of observation from which 5,178 dipolarizations are identified. This event sample size is
218 an order of magnitude larger than previously examined at Mercury (e.g., Dewey et al., 2018) and allows
219 us to employ statistical techniques to examine the characteristics of dipolarizations as a function of
220 spatial location in Mercury's magnetotail (Section 3).

221

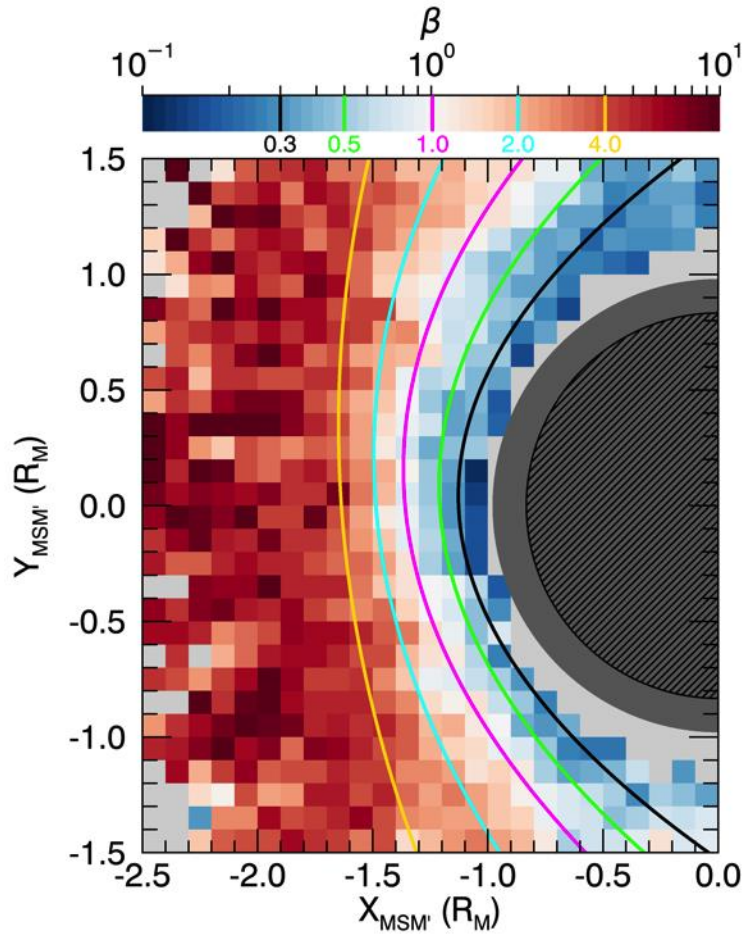


Figure 1. Equatorial distribution of proton plasma beta (β) as indicated by the color bar. Light grey bins indicate regions of insufficient sampling (<6 FIPS scans, corresponding to <2 min of sampling). The dark grey indicates Mercury's nightside surface and the black-hatched region denotes its conducting core. The five color polynomials (black, lime, magenta, cyan, and gold) are contours of specific β (0.3, 0.5, 1.0, 2.0, and 4.0), as indicated by the vertical lines of the corresponding color in the color bar.

To provide context to the dipolarization observations described in later sections, we determine the average proton plasma beta (β) as a function of spatial location in Mercury's magnetic equatorial plane, as shown in Figure 1. To construct this distribution, we compute the average magnetic field, proton density, and proton temperature under the assumption of isotropy (e.g., Raines et al., 2011; Gershman et al., 2013) for each FIPS scan within the 1,946 intervals (84,187 scans total). We then use the spacecraft's location at the center of each scan to sort scans into a two dimensional ($X_{MSM'}$, $Y_{MSM'}$) histogram. Within each histogram bin, we determine the mean proton density, proton temperature, and magnetic field strength from the scans assigned to that bin, from which plasma beta is then calculated. We propagate uncertainties, which are typically on the order of 1-5% for magnetic field strength and 10-20% for proton density and temperature. For five specific values of β (0.3, 0.5, 1.0, 2.0, and 4.0) we determine contours within the spatial distribution and display polynomial fits to those contours (black, lime, magenta, cyan, and gold, respectively). Each contour is well represented by a second-order polynomial (χ^2 values of 0.045, 0.049, 0.029, 0.033, and 0.019, respectively). As expected for the plasma sheet, $\beta \gg 1$ far from the center of the planetary dipole with contours nearly parallel to $Y_{MSM'}$. Approaching the planet, β decreases and contours bow about the planetary magnetic field, with $\beta \ll 1$ close the dipole center. For reference, at local midnight, $\beta = 1$ (magenta line) at $X_{MSM'} \approx -1.36 R_M$,

246 approximately 900 km in altitude above the nightside surface. Plasma beta also displays a cross-tail
247 asymmetry, with systematically greater values in the post-midnight plasma sheet. This asymmetry can
248 be observed by noticing that the β contours in the post-midnight plasma sheet are located at greater
249 $X_{\text{MSM}'}$ values than those in the pre-midnight plasma sheet. For example, at $Y_{\text{MSM}'} = -1 R_M$ the $\beta = 1$
250 contour is located at $X_{\text{MSM}'} \approx -0.98 R_M$ while at $Y_{\text{MSM}'} = +1 R_M$ the same contour is located at $X_{\text{MSM}'} \approx -$
251 $1.16 R_M$. This cross-tail asymmetry is among other asymmetries noted in plasma and magnetic field
252 parameters in Mercury's central plasma sheet (e.g., Raines et al., 2013; Korth et al., 2014; Poh et al.,
253 2017b; Rong et al., 2018).

254

255 3. Results

256 3.1 Observations of flow braking

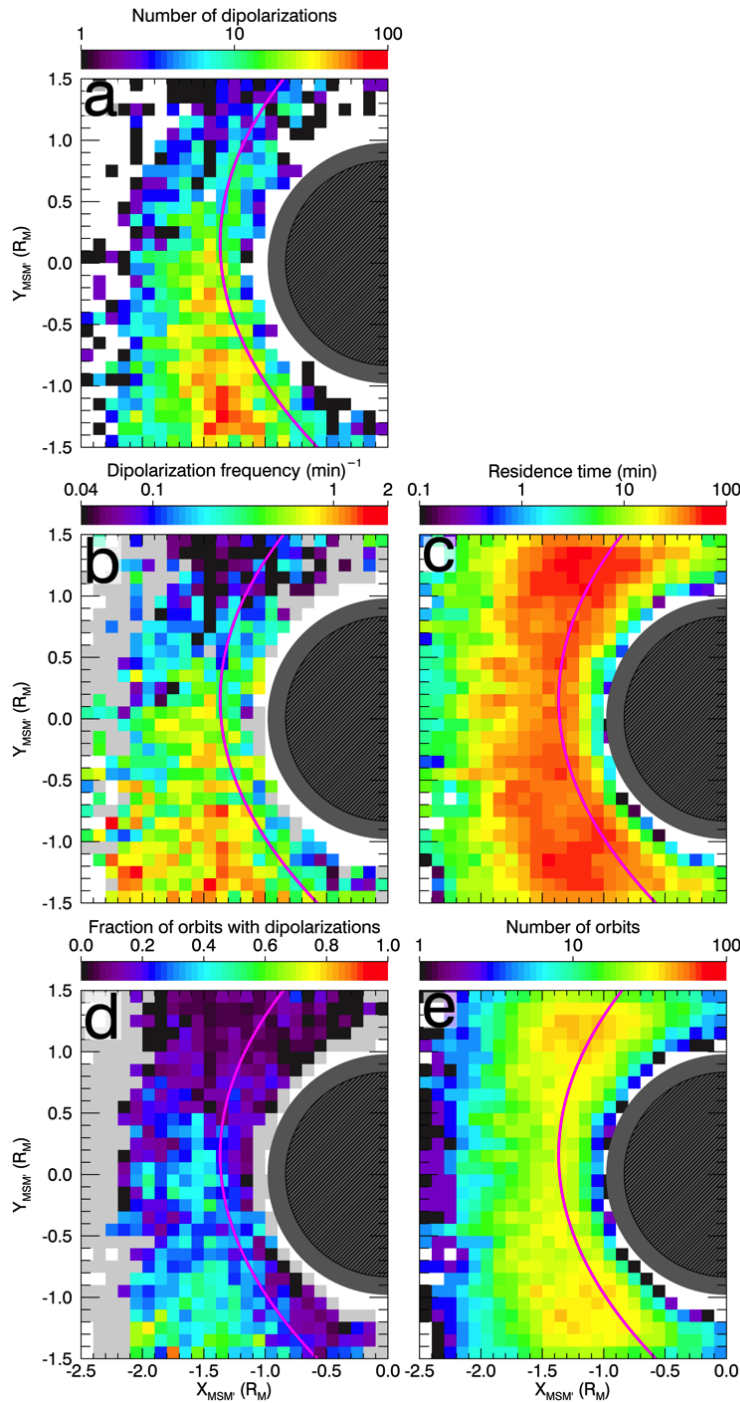
257

258 To determine if dipolarizations impact Mercury's nightside surface directly or if they brake/divert before
259 then, we begin by examining the distribution of dipolarization occurrence as a function of location
260 within Mercury's magnetotail. Figure 2a displays the number of dipolarizations identified by the
261 automated procedure of Section 2 as a function of equatorial ($X_{\text{MSM}'}$, $Y_{\text{MSM}'}$) location. As a function of
262 $Y_{\text{MSM}'}$, dipolarizations display a strong cross-tail asymmetry with over an order of magnitude more
263 dipolarizations observed post-midnight than pre-midnight similar to the findings of other studies (Sun et
264 al., 2016; Dewey et al., 2018). The range $-1.5 < Y_{\text{MSM}'} < 0.5 R_M$ contains 90.7% of the identified
265 dipolarizations. As a function of $X_{\text{MSM}'}$, the number of dipolarizations drops sharply planetward of the β
266 $= 1$ contour (magenta line), particularly in the post-midnight magnetotail. Few dipolarizations are
267 observed tailward of $X_{\text{MSM}'} = -2 R_M$.

268

269 To account for effects from non-uniform spacecraft sampling, we display the frequency of
270 dipolarizations within Figure 2b. To produce this distribution, we divide the number of dipolarizations
271 observed within each spatial bin (Figure 2a) by the total time the spacecraft was at that location during
272 the 1,946 intervals (Figure 2c). Examining the frequency of dipolarizations, the strong cross-tail
273 asymmetry persists. The apparent decrease in dipolarizations tailward of $X_{\text{MSM}'} = -2 R_M$, however, is
274 removed after correcting for spacecraft sampling. Dipolarizations possess an approximately uniform
275 frequency tailward of the $\beta = 1$ contour for $Y_{\text{MSM}'} < -0.5 R_M$. The decrease in number of dipolarizations
276 sunward of $\beta = 1$ does not appear to be an artifact of spacecraft sampling. Where dipolarizations are
277 most frequent ($-1.5 < Y_{\text{MSM}'} < 0.5 R_M$), the frequency decreases by an order of magnitude about $\beta = 1$.
278 For $Y_{\text{MSM}'} < -0.5 R_M$, the frequency tailward of $\beta = 1$ is ~ 1 -2 dipolarizations per minute, falling to ~ 0.1 -
279 0.2 closer to the planet. The trend is less clear at local midnight ($-0.5 < Y_{\text{MSM}'} < 0.5 R_M$). The frequency
280 tailward of $\beta = 1$ is ~ 1 dipolarization per minute, and while there are several bins planetward of $\beta = 1$
281 that reach similar frequencies, there is considerable scatter, with many bins observing dipolarizations at
282 a rate of ~ 0.2 per minute and many others observing no dipolarizations at all (light grey).

283



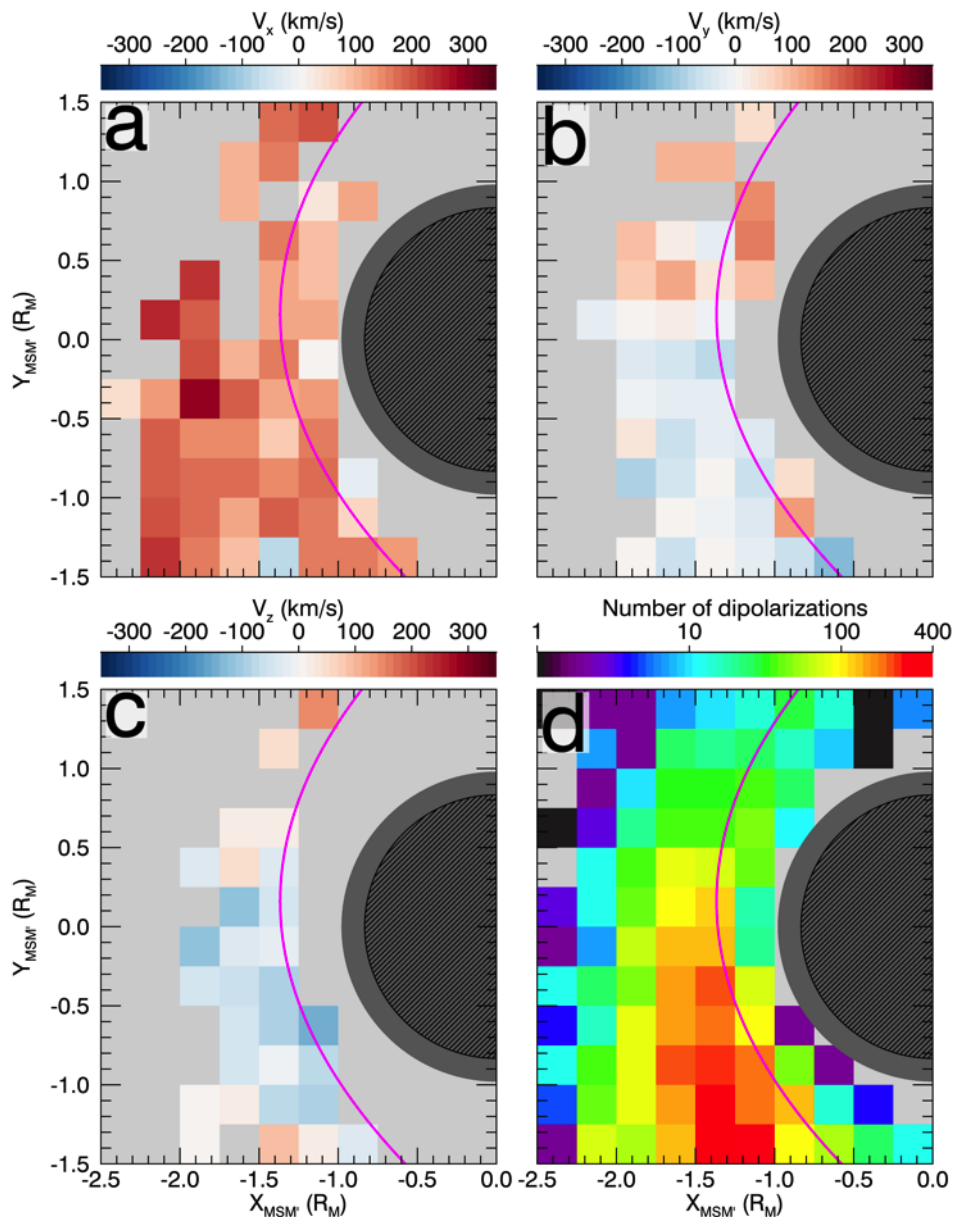
284
285
286
287
288
289
290
291
292
293
294

Figure 2. Equatorial distributions in the same format as Figure 1. (a) Number of dipolarizations, where white indicates no dipolarizations observed. (b) Frequency of dipolarizations, where light grey indicates no dipolarizations observed and white indicates insufficient sampling time (<1 min). (c) Spacecraft sampling time, where white indicates regions of no samples. (d) Fraction of orbits that contain dipolarizations within that spatial bin, where light grey indicates insufficient sampling (<3 orbits) and white indicates regions of no sampling. (e) Number of orbits, where white indicates regions of no samples. The magenta polynomial in each panel corresponds to the $\beta = 1$ contour from Figure 1.

295 As will be described in further detail below (Figure 7), when dipolarizations are observed, they tend to
296 be observed in series with other dipolarizations. This trend has been anecdotally described in other
297 studies involving dipolarizations at Mercury (e.g., Sundberg et al., 2012; Dewey et al., 2017; Dewey et
298 al., 2018; Sun et al., 2020). An effect of dipolarizations typically appearing in groups is that it can skew
299 event frequency. We therefore use the fraction of orbits that contain dipolarizations (Figure 2d) as a
300 metric complementary to event frequency. To produce this distribution, for each spatial bin, we
301 determine the number of orbits that contain one or more dipolarizations within that bin and divide it by
302 the total number of orbits that sampled that bin (Figure 2e). Similar to conventional frequency (Figure
303 2b), the cross-tail asymmetry in dipolarization occurrence persists. Post-midnight, a greater fraction of
304 orbits (~ 0.4 - 0.7) contain dipolarizations than pre-midnight (~ 0.1). About $\beta = 1$, the fraction of orbits that
305 contain dipolarizations also drops substantially. Where dipolarizations are most common ($-1.5 < Y_{\text{MSM}'} < 0.5 R_M$),
306 the fraction of orbits with dipolarizations decreases from ~ 0.4 - 0.5 just tailward of $\beta = 1$ to
307 ~ 0.1 planetward of the contour. The only location within this $Y_{\text{MSM}'}$ range that does not appear to follow
308 this trend is at $Y_{\text{MSM}'} = -0.5 R_M$ where the fraction of orbits with dipolarizations (~ 0.4) remains
309 unchanged about $\beta = 1$.

310
311 Taken together, these trends in dipolarization occurrence imply that they do not typically reach
312 Mercury's nightside surface. If dipolarizations usually impacted the planet, we should expect the rate at
313 which dipolarizations are observed to remain approximately constant up to the planet's surface. Rather,
314 we observe that the rate of dipolarization occurrence (interpreted either as the frequency of
315 dipolarizations or as the fraction of orbits that contain dipolarizations) decreases sharply about the $\beta = 1$
316 contour, which is located ~ 900 km altitude above the nightside surface. If dipolarizations do indeed
317 divert or brake before reaching the nightside surface, these signatures should be apparent in the flows
318 associated with dipolarizations. As described in Section 2, FIPS cannot determine flows at its nominal
319 time resolution, however, we can follow the procedure developed by Dewey et al. (2018) to examine
320 flows statistically. We refer readers to Dewey et al. (2018) for technical details of this procedure. While
321 Dewey et al. (2018) used 387 dipolarizations spread throughout Mercury's magnetotail to obtain a single
322 representative flow, we can leverage our increased event sample size to determine statistical flows as a
323 function of spatial location, enabling us to examine plasma signatures of flow breaking.

324
325 In Figure 3, we apply the Dewey et al. (2018) flow-determination technique to FIPS observations of
326 dipolarizations. For each spatial bin, we first identify all dipolarizations that were observed within that
327 area of the magnetotail, then we select all FIPS scans that cover the end of each of those event's
328 dipolarization fronts, and finally, we apply the Dewey et al. (2018) technique to those scans to determine
329 average flows. Figure 3a displays the sunward component of these flows (V_x), 3b the duskward
330 component (V_y), 3c the northward component (V_z), and 3d the number of dipolarizations. In calculating
331 these statistical flows, we evaluate uncertainty from statistical and systematic sources as well as
332 uncertainty resulting from unobserved regions of velocity space (see Appendix B and Dewey et al.,
333 2018). While some spatial bins in 3d have up to 400 dipolarizations, many have between 50-100. The
334 number of dipolarizations used to determine statistical flows is smaller on average than that used by
335 Dewey et al. (2018), which results in larger uncertainties as well as prevents some flow components
336 from being reliably determined (grey bins in Figures 3a-c). In Appendix B, we describe quantitatively
337 the conditions under which we do not display flow components. Including each of the sources of
338 uncertainty described above, typical absolute and relative uncertainties for each velocity component
339 shown in Figure 3 are 32 ± 9 km/s or $(25 \pm 7)\%$ in V_x , 22 ± 10 km/s or $(47 \pm 22)\%$ in V_y , and 15 ± 8
340 km/s or $(35 \pm 19)\%$ in V_z . Finally, we expect proton flows to be representative of dipolarization
341 transport. Dipolarizations have dimensions $\sim 2,000$ km in $X_{\text{MSM}'}$ and ~ 750 km in $Y_{\text{MSM}'}$ (see Section 3.3),
342 which are greater than the typical proton gyroradius about dipolarizations (~ 300 km for a 4 keV proton
343 in a 30 nT magnetic field), indicating that the frozen-in condition is valid.



345
 346 **Figure 3.** Typical dipolarization flow components as a function of equatorial location in the
 347 same format as Figure 2. (a) Sunward component (V_x), (b) duskward component (V_y), (c)
 348 northward component (V_z), and (d) number of dipolarizations used to determine these flows.
 349 Light grey bins in (a)-(c) indicate spatial locations whose flow component in that direction could
 350 not be determined reliably (see Appendix B). Light grey bins in (d) indicate regions with no
 351 dipolarizations.
 352

353 The flows in Figure 3 are indicative of both flow braking and diversion. Tailward of $\beta = 1$, V_x is
 354 dominant with speeds around 200 km/s in the sunward direction, similar to the dipolarization flow
 355 determined by Dewey et al. (2018). V_y shows a general separation about midnight tailward of $\beta = 1$
 356 although there is considerable scatter. The mean, median, and standard deviation of V_y flows pre-
 357 midnight is 89, 59, and 97 km/s, respectively, compared to -59 , -54 , and 66 km/s post-midnight. A
 358 linear fit of V_y versus Y_{MSM} yields a slope of 38 ± 4 km/s R_M^{-1} with a correlation coefficient of 0.62.
 359 The large variance amongst V_y flows suggests that V_y can vary substantially between individual

360 dipolarizations but with a general trend of $+V_y$ flows pre-midnight and $-V_y$ flows post-midnight. Flows
361 along Z_{MSM} are generally negative about local midnight and positive closer to the flanks of the
362 magnetotail, and are of the same approximate strength as V_y . Planetward of $\beta = 1$, the sunward
363 component decreases in magnitude. This trend is most apparent for $-1 < Y_{MSM} < 0 R_M$, where V_x
364 decreases from ~ 100 - 200 km/s to ~ 0 - 50 km/s about $\beta = 1$. While V_z cannot be reliably determined
365 planetward of $\beta = 1$, the V_y appears to become systematically duskward with an average value of $53 \pm$
366 31 km/s. These V_x and V_y flow signatures are indicative of both flow braking and diversion.

367
368 Figure 4 displays trends along X_{MSM} more clearly. Each panel examines plasma or magnetic field
369 parameter(s) averaged over $-1.5 < Y_{MSM} < 0.5 R_M$ (where dipolarizations are most common) as a
370 function of ΔX_{MSM} . ΔX_{MSM} is the distance along X_{MSM} from the $\beta = 1$ contour (i.e., $\Delta X_{MSM} = 0$ lies on
371 the $\beta = 1$ contour, with $\Delta X_{MSM} > 0$ planetward of the contour). Figure 4a examines the frequency of
372 dipolarizations organized by ΔX_{MSM} . Similar to the observations discussed with Figure 2, the frequency
373 of dipolarizations remains approximately constant until $\beta = 1$. For $-1.5 < \Delta X_{MSM} < 0 R_M$, the
374 dipolarization frequency fluctuates but remains about 0.6 min^{-1} (shaded grey region) until decreasing
375 significantly at $\Delta X_{MSM} \approx 0$. By the $\beta = 0.5$ contour (lime), the frequency has dropped to half its downtail
376 value. Further planetward, the frequency continues to drop to $\sim 0.1 \text{ min}^{-1}$, suggesting that only a small
377 fraction (~ 10 - 20%) of dipolarizations may impact the nightside surface directly. The sunward flow
378 component V_x in Figure 4b displays a similar trend. For $-1.5 < \Delta X_{MSM} < 0 R_M$, the sunward flow speed
379 fluctuates but remains about 192 km/s (horizontal dashed line) before beginning to decrease
380 meaningfully at $\Delta X_{MSM} \approx 0$. By the $\beta = 0.5$ contour, the sunward flow has decreased to approximately
381 half its downtail value. The dipolarization frequency and flow speed decreasing to half their respective
382 downtail values by $\Delta X_{MSM} \approx 0.15 R_M$ suggests the braking region has a downtail extent of ~ 500 km and
383 begins at $\beta = 1$ (an altitude of ~ 900 km at local midnight).

384
385 To understand the mechanism causing braking to occur in Mercury's magnetotail, Figure 4c examines
386 proton plasma pressure and magnetic pressure as functions of ΔX_{MSM} . We follow the same general
387 procedure in determining these pressures as for the proton plasma beta within Section 2. In order to
388 examine conditions that dipolarizations encounter, we use only FIPS and MAG measurements belonging
389 to orbits that contain one or more dipolarization. For $\Delta X_{MSM} < 0$, both plasma and magnetic pressures
390 remain small (< 1 nPa) with the plasma pressure dominating magnetic pressure (consistent with $\beta > 1$).
391 At $\Delta X_{MSM} = 0$, both pressures are within uncertainty of each other ($\beta = 1$). For $\Delta X_{MSM} > 0$, magnetic
392 pressure dominates plasma pressure ($\beta < 1$) as we move closer to Mercury's dipole center. Using these
393 one-dimensional pressure profiles, we can estimate the pressure gradient forces in the sunward direction.
394 For both $\Delta X_{MSM} < 0$ and $\Delta X_{MSM} > 0$, we apply linear fits to both the magnetic and plasma pressure
395 profiles with the slope of the fit indicating the force density. For $\Delta X_{MSM} < 0$, both magnetic and plasma
396 pressure gradients are small (~ 0.1 - 0.2 nPa R_M^{-1}) and are within uncertainty of each other. At $\Delta X_{MSM} =$
397 0 , the magnetic pressure gradient increases by a factor of 60 ± 20 and the plasma pressure gradient
398 increases by a more modest factor of 16 ± 7 . The strong pressure gradients, particularly in magnetic
399 pressure, coincident with the decreases in dipolarization occurrence and flow speed suggest
400 dipolarizations and their associated fast flows brake as a result of the strong magnetic pressure gradients
401 of Mercury's dipole magnetic field. Finally, Figure 4d displays the local Alfvén speed (V_A) as a function
402 of ΔX_{MSM} . We do not incorporate heavy planetary ion species (e.g., Na^+) in calculating the V_A and find
403 that including them would not reduce V_A significantly. We will use V_A in the discussion of current
404 wedge formation in Section 4. For now, we illustrate that dipolarizations far downtail of the braking
405 region ($\Delta X_{MSM} < -1 R_M$) typically travel near the local Alfvén speed, consistent with magnetic
406 structures created from magnetic reconnection.

407

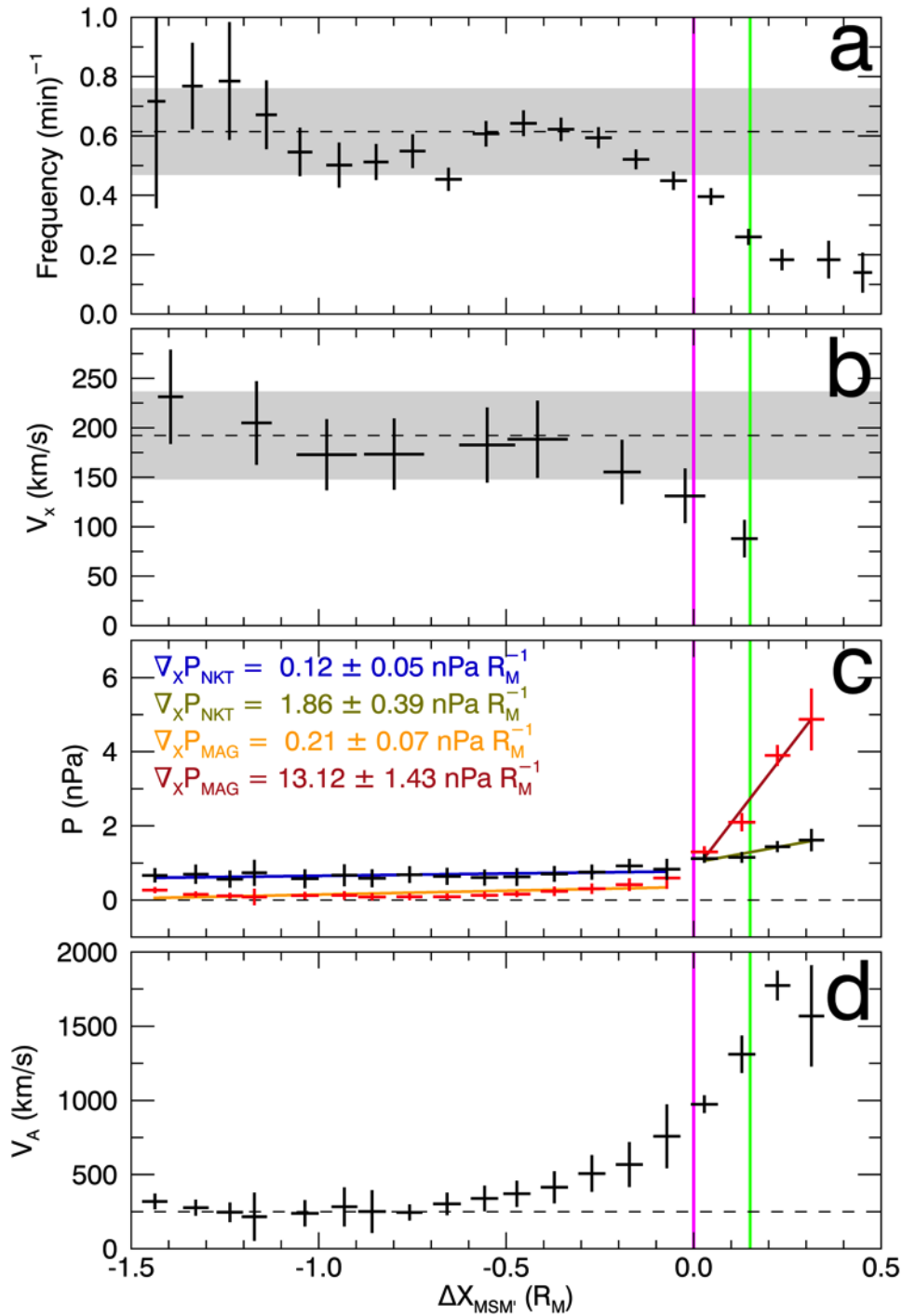


Figure 4. (a) Dipolarization frequency, (b) typical dipolarization sunward flow, (c) magnetic (P_{MAG}) and thermal proton (P_{NKT}) pressures, and (d) Alfvén speed as functions of $\Delta X_{\text{MSM}'}$ (defined in the text). The vertical magenta line corresponds to the location of the $\beta = 1$ contour and the vertical lime line corresponds to the location of the $\beta = 0.5$ contour (see Figure 1). In (a) and (b), the horizontal dashed lines and grey boxes correspond to the average and uncertainty of dipolarization frequency and sunward flow speed for $-1.5 < \Delta X_{\text{MSM}'} < 0 R_M$. In (c), the horizontal dashed line corresponds to a pressure of zero, while the colored lines correspond to linear fits whose slopes are listed. In (d), the horizontal dashed line corresponds to a speed of 250 km/s.

408
409
410
411
412
413
414
415
416
417
418

419
420
421

3.2 Observations of flux pileup

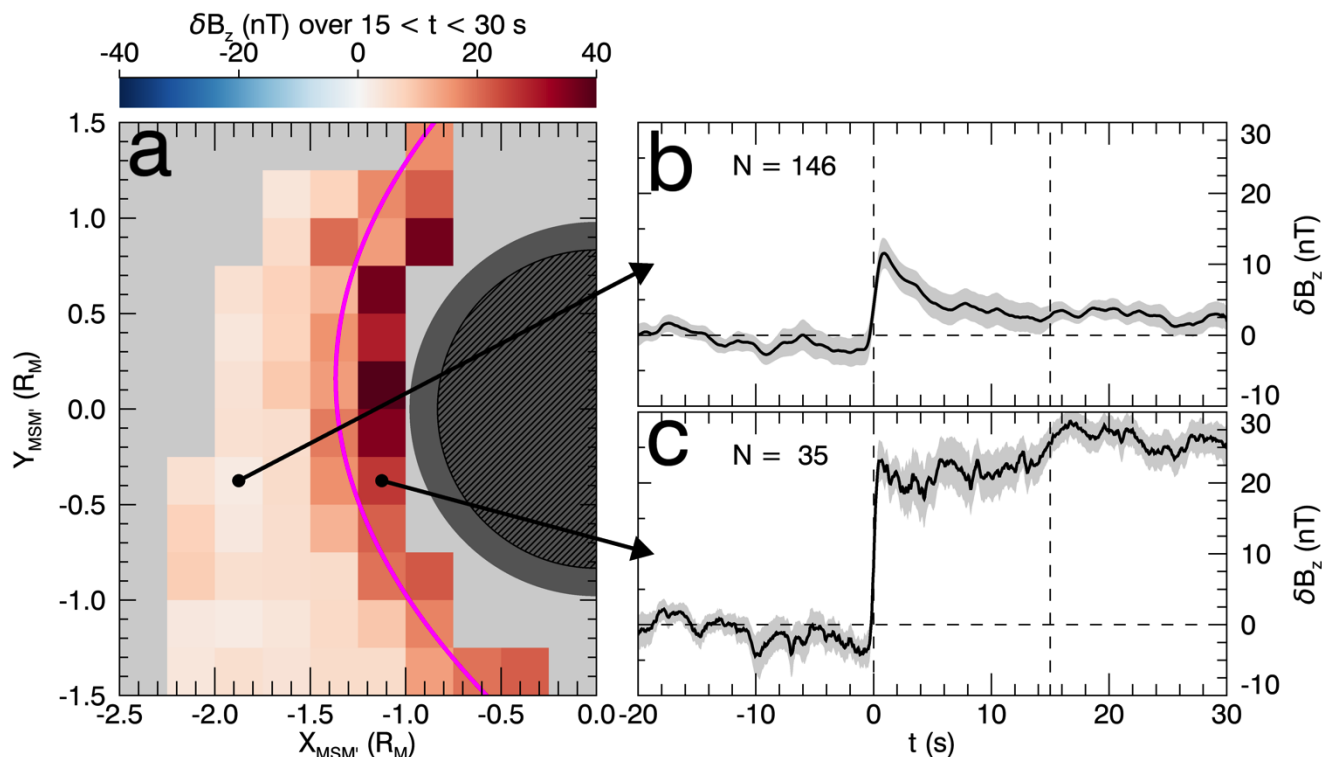


Figure 5. (a) Equatorial distribution of the average detrended, background-subtracted northward magnetic field component (δB_z) following dipolarizations in the same format as Figure 3. The color bar indicates the average δB_z of the superposed dipolarization profiles over $15 < t < 30$ s. Light grey regions have insufficient number of dipolarizations for statistical analysis (< 15 dipolarizations, see Figure 3d). The black arrows indicate corresponding spatial locations in (a) for the two example profiles in (b) and (c). For (b) and (c), the thick black line indicates the mean δB_z over the N -dipolarizations at each time step and the light grey indicates the standard error. The vertical dashed lines correspond to $t = 0$ s (the midpoint of dipolarization fronts that the profiles are organized by) and $t = 15$ s. The horizontal dashed lines correspond to 0 nT.

Observations of dipolarization frequency and flow speed in Section 3.1 establish that dipolarizations typically brake before reaching Mercury's nightside surface. Within this section, we investigate whether the flow braking of dipolarizations is associated with magnetic flux pileup. We begin by first examining dipolarization profiles as a function of location within Mercury's magnetotail, similar to the frequency maps of Figure 2 and the flow maps of Figure 3. In Figure 5, we examine the northward component of the magnetic field (B_z) following dipolarizations. We standardize dipolarizations by converting to new time and magnetic field coordinates. For time, we use t , which is the time in seconds local to the midpoint of a dipolarization's dipolarization front (i.e., the midpoint of a dipolarization front is defined to be $t = 0$ s). For the magnetic field, we are interested in how the field changes after the dipolarization compared to before it, so we define $\delta \mathbf{B}$, the background-subtracted, detrended magnetic field. To construct $\delta \mathbf{B}$, we first remove the effects of the spacecraft's motion through Mercury's dipole magnetic field after which we subtract the average magnetic field over $-20 < t < -10$ s. Using the same spatial gridding as in Figure 3, we examine the superposed epoch profiles of dipolarizations in the new ($t, \delta B_z$) coordinates as a function of equatorial location.

447

448 The average δB_z over $15 < t < 30$ s from each spatially-resolved superposed dipolarization profile is
 449 shown in Figure 5a, while Figures 5b and 5c show two example profiles, one tailward and one
 450 planetward of the $\beta = 1$ contour, respectively. Tailward of $\beta = 1$, dipolarizations do not exhibit large,
 451 prolonged enhancements of the magnetic field following the initial dipolarization. In Figure 5b, for
 452 example, the magnetic field decreases slightly prior to the sharp, step-like increase of the dipolarization
 453 front (centered at $t = 0$) after which the northward component of the magnetic field remains enhanced
 454 for several seconds before falling to near pre-dipolarization values. The average δB_z over $15 < t < 30$ s
 455 remains close to within uncertainty of the value over $-20 < t < -10$ s. Correspondingly, the average δB_z
 456 over $15 < t < 30$ s for regions tailward of $\beta = 1$ in Figure 5a is small, $\lesssim 5$ nT. In contrast, dipolarizations
 457 at and planetward of $\beta = 1$ display substantial, prolonged increases in the magnetic field. The superposed
 458 dipolarization profile in Figure 5c, for example, shares similar features as the profile in Figure 5b,
 459 however, after the initial dipolarization front, the magnetic field remains enhanced by ~ 25 nT for a
 460 substantial duration of time (i.e., greater than the typical dipolarizing flux bundle duration of ~ 10 s, see
 461 Dewey et al., 2017). Correspondingly, the average post-dipolarization δB_z at and planetward of the $\beta = 1$
 462 contour in Figure 5a has values ~ 10 - 40 nT, with a median value of 29 nT. Planetward of $\beta = 1$, the post-
 463 dipolarization δB_z is asymmetric about local midnight, with greater strength pre-midnight (~ 36 nT) than
 464 post-midnight (~ 26 nT). Synoptically, the prolonged δB_z enhancement planetward of $\beta = 1$ appears to be
 465 a large-scale dipolarization of Mercury's near-tail region.

466
 467 These spatially-resolved superposed dipolarization profiles indicate flux pileup occurs in Mercury's
 468 magnetotail alongside flow braking. Tailward of $\beta = 1$, superposed dipolarization profiles exhibit only
 469 transient increases in the magnetic field consistent with dipolarizations travelling rapidly sunward and
 470 passing quickly over the spacecraft and resulting in a small δB_z over $15 < t < 30$ s. Planetward of $\beta = 1$,
 471 coincident with where substantial braking occurs, the superposed dipolarization profile indicate a more
 472 permanent increase in the magnetic field with magnetic flux pileup resulting in a large average δB_z over
 473 $15 < t < 30$ s. To determine if the synoptic pileup (i.e., large-scale dipolarization) signature across
 474 Mercury's near-tail region is physical, we turn to magnetic flux budget analysis in Section 3.3 and
 475 examine a case study in Section 3.4.

476 477 **3.3 Flux budget of statistical pileup signature**

478
 479 To determine if the statistical, synoptic flux pileup signature (i.e., large-scale dipolarization) is physical,
 480 we first look to determine if dipolarizations could supply sufficient magnetic flux to establish it. We
 481 integrate δB_z in Figure 5a planetward of $\beta = 1$ and within $|Y_{\text{MSM}}| < 1.25 R_M$ to estimate that the large-
 482 scale flux pileup contains 0.28 ± 0.08 MWb magnetic flux. We wish to determine if it is possible for
 483 dipolarizations to supply this flux to the inner magnetotail.

484
 485 The typical magnetic flux transported by a dipolarization can be estimated by

$$486 \quad \Phi \approx 2\Delta Y V_x \int B_z dt$$

487 where ΔY is the half-width of the dipolarization, assumed to be approximately constant. We can use
 488 superposed dipolarization profiles and typical dipolarization flows to estimate these terms, however, the
 489 cross-tail half-width remains unknown. Determining the width of dipolarizations is challenging, even
 490 when multi-spacecraft observations available (e.g., Sergeev et al., 1996; Nakamura et al., 2004).
 491 However, taking advantage of our expanded dipolarization event list, we can employ statistical
 492 techniques to provide some insight into their cross-tail width. Similar to determining dipolarization
 493 flows, we will not be able to determine the cross-tail width of dipolarizations on an event-by-event basis,
 494 but rather, we can use the following statistical analysis to determine a representative value.

495

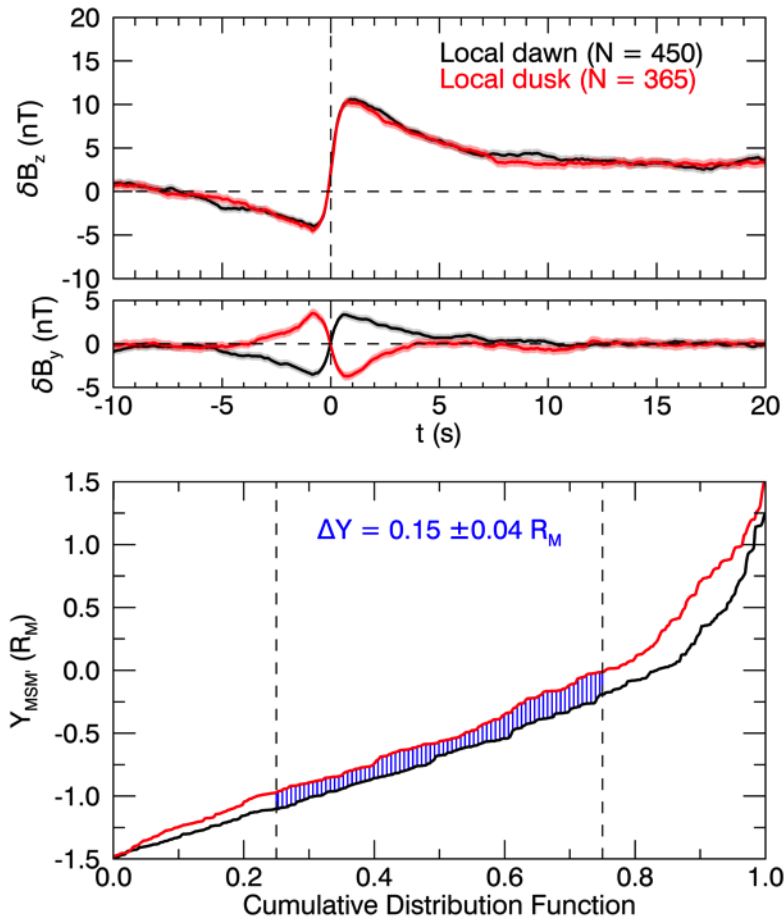


Figure 6. (top) Superposed dipolarization profiles of δB_z and δB_y for dipolarizations observed at their local dawn (black) and local dusk (red) sides in the same format as Figure 5b and 5c. (bottom) Cumulative distribution function of the spacecraft $Y_{MSM'}$ location when it encountered a dipolarization on the dipolarization's local dawn (black) or local dusk (red) side. The separation between the curves (vertical blue lines) indicates the typical cross-tail half-width of dipolarizations. The dashed vertical black lines indicate the 25th and 75th percentiles.

496 Dipolarizations possess several current structures (e.g., Sun et al., 2013). At the dipolarization front, a
 497 dawn-to-dusk current separates the surrounding plasma from the enhanced B_z within the dipolarization.
 498 While some of this current closes about the dipolarization, most is expected to close as field-aligned
 499 currents of the Region-2 sense (e.g., Birn et al., 2019). These field-aligned currents produce
 500 perturbations in the magnetic field that we can use to determine if the spacecraft observed the local
 501 dawn or dusk flank of the dipolarization. For example, for spacecraft observations of the local dawn
 502 side of dipolarizations whose field-aligned current closes into the northern hemisphere, we expect a negative-
 503 then-positive perturbation in B_y (i.e., $\delta B_y < 0$ followed by $\delta B_y > 0$) at the dipolarization front. By
 504 examining the distribution of where the spacecraft observed the local dawn versus local dusk sides of
 505 dipolarizations, we can determine the characteristic cross-tail width. For example, consider if
 506 dipolarizations at Mercury typically encompass the entire width of the magnetotail ($-2 < Y_{MSM'} < 2 R_M$).
 507 Observing the local dawn side would only occur when the spacecraft is post-midnight ($Y_{MSM'} < 0$), and
 508 observing the local dusk side would only occur when the spacecraft is pre-midnight ($Y_{MSM'} > 0$). The
 509 typical separation between observations of local dawn (on average, $Y_{MSM'} \approx -1 R_M$) and of local dusk
 510 (on average, $Y_{MSM'} \approx 1 R_M$) would be $2 R_M$, the half-width of the full structure ($4 R_M$).
 511
 512
 513
 514
 515
 516
 517
 518
 519

520 We implement this methodology to determine the typical dipolarization half-width ΔY in Figure 6. We
521 select dipolarizations in the $\beta > 1$ region (to avoid contamination from braking dipolarizations) that
522 possess significant bipolar signatures in δB_y at the dipolarization front. We use the polarity of the δB_y
523 signature and the spacecraft's Z_{MSM} location to estimate if the spacecraft observed the local dawn or
524 local dusk side of the event. A total of 815 dipolarizations met these criteria, with the spacecraft
525 observing local dawn for 450 of these events, and local dusk for the remaining 365. The top panels of
526 Figure 6 display the superposed epoch δB_z and δB_y profiles of these events. We invert the sign of δB_y
527 for events when $Z_{MSM} < 0$ to produce clear signals in the superposed δB_y profiles (i.e., for events with
528 $Z_{MSM} < 0$, we display $-\delta B_y$ in Figure 6). The profiles look nearly identical in magnitude and timing,
529 with just the polarity of the δB_y bipolar signature reversed. The bottom panel displays the cumulative
530 distribution function of the spacecraft's Y_{MSM} position for both local dawn (black) and local dusk (red)
531 observations. As expected, the spacecraft position is systematically shifted to greater Y_{MSM} when it
532 observed dipolarizations' local dusk side. The separation between the two distribution functions
533 indicates the typical dipolarization half-width. To avoid outliers, we use the 25th to 75th percentiles
534 (dashed vertical lines) to estimate $\Delta Y = 0.15 \pm 0.04 R_M$. We combine the dipolarization half-width with
535 the Figure 6a B_z profiles and the average downtail V_x flow (192 ± 44 km/s; the horizontal dashed line in
536 Figure 4a) to estimate that a single dipolarization typically transports 0.053 ± 0.019 MWb.

537
538 To supply the magnetic flux observed in the flux pileup region would therefore require 5 ± 2
539 dipolarizations. The number of dipolarizations required to build the flux pileup signature is supported
540 observationally, shown in Figure 7. Figure 7a displays the number of dipolarizations identified during an
541 orbit versus the median time between those dipolarizations (time between successive dipolarization
542 fronts). We include the time between dipolarizations as it suggests a causal link; dipolarizations
543 separated by >2 -3 min, for instance, may not be considered to be of the same substorm. Figure 7b shows
544 the marginal distribution of the number of dipolarizations observed per orbit, while Figure 7c shows the
545 time between individual dipolarization fronts (as opposed to the median separation time per orbit in 7a).
546 From Figure 7b, nearly half of orbits (818/1946 ~ 0.4) contain no dipolarizations. Of the remaining
547 orbits, more orbits contain more than one dipolarization than a single dipolarization. Approximately
548 $\sim 18\%$ of all orbits (345/1946) contain 5 or more dipolarizations, with the most extreme containing 32.
549 Examining the time between dipolarizations (Figure 7c), most dipolarizations are observed in series with
550 one followed soon by another. The typical time between dipolarization fronts is between 5-20 s while
551 the typical dipolarization duration is ~ 10 s (Dewey et al., 2017). Combining these distributions together
552 in Figure 7a, only $\sim 6\%$ of orbits contain a sufficient number of dipolarizations (5) with median time
553 between dipolarizations < 20 s. While this is a small fraction of orbits, this determination is sensitive to
554 the number of active reconnection sites in Mercury's magnetotail (e.g., if two reconnection sites are
555 active we may require the spacecraft to observe 2-3 dipolarizations for the orbit to qualify). We do not
556 intend this fraction of orbits to communicate how common large-scale pileup may occur, but rather that
557 the flux pileup signature identified statistically in Figure 5 is indeed possible to establish via multiple
558 dipolarizations.

559

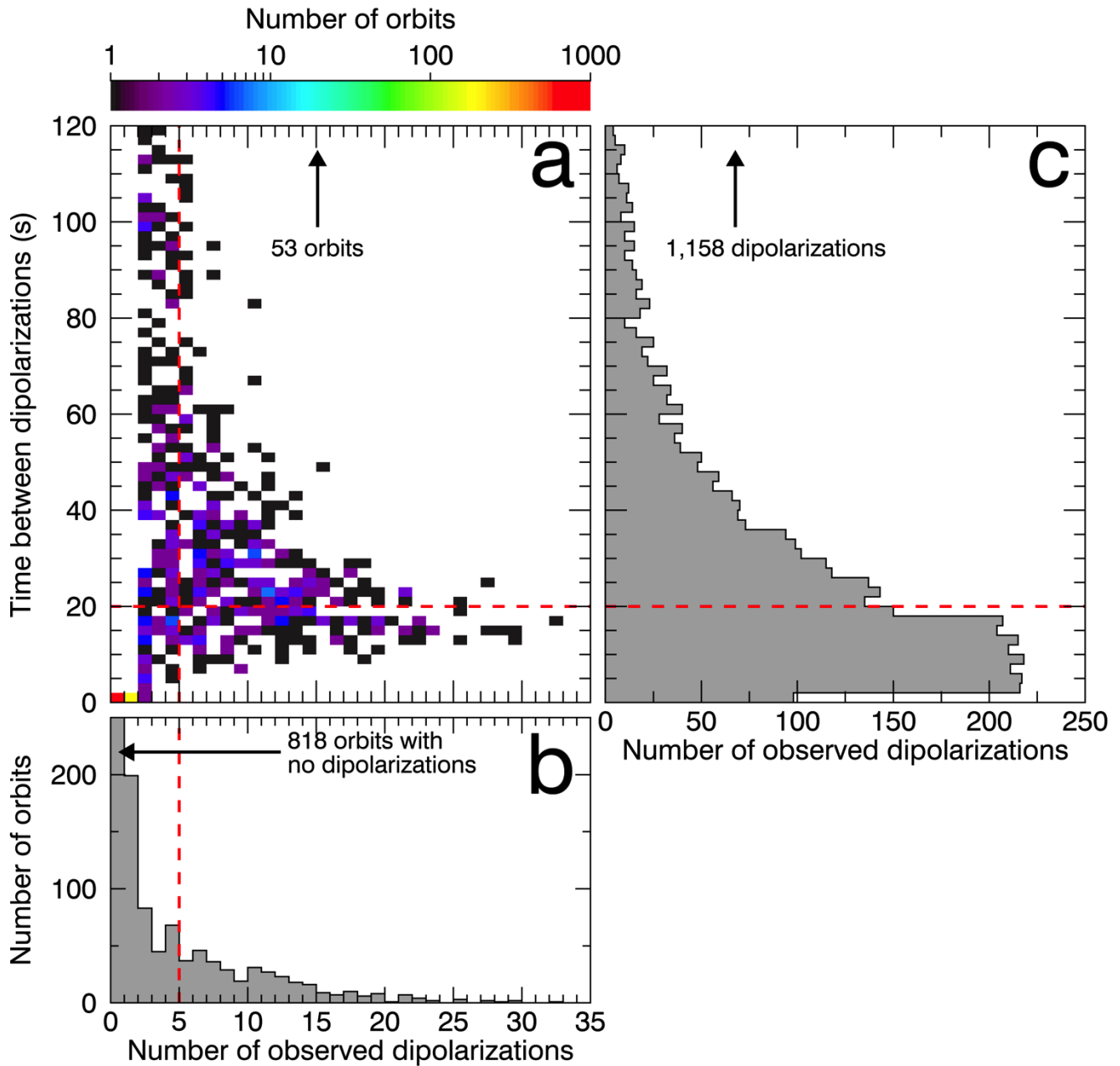
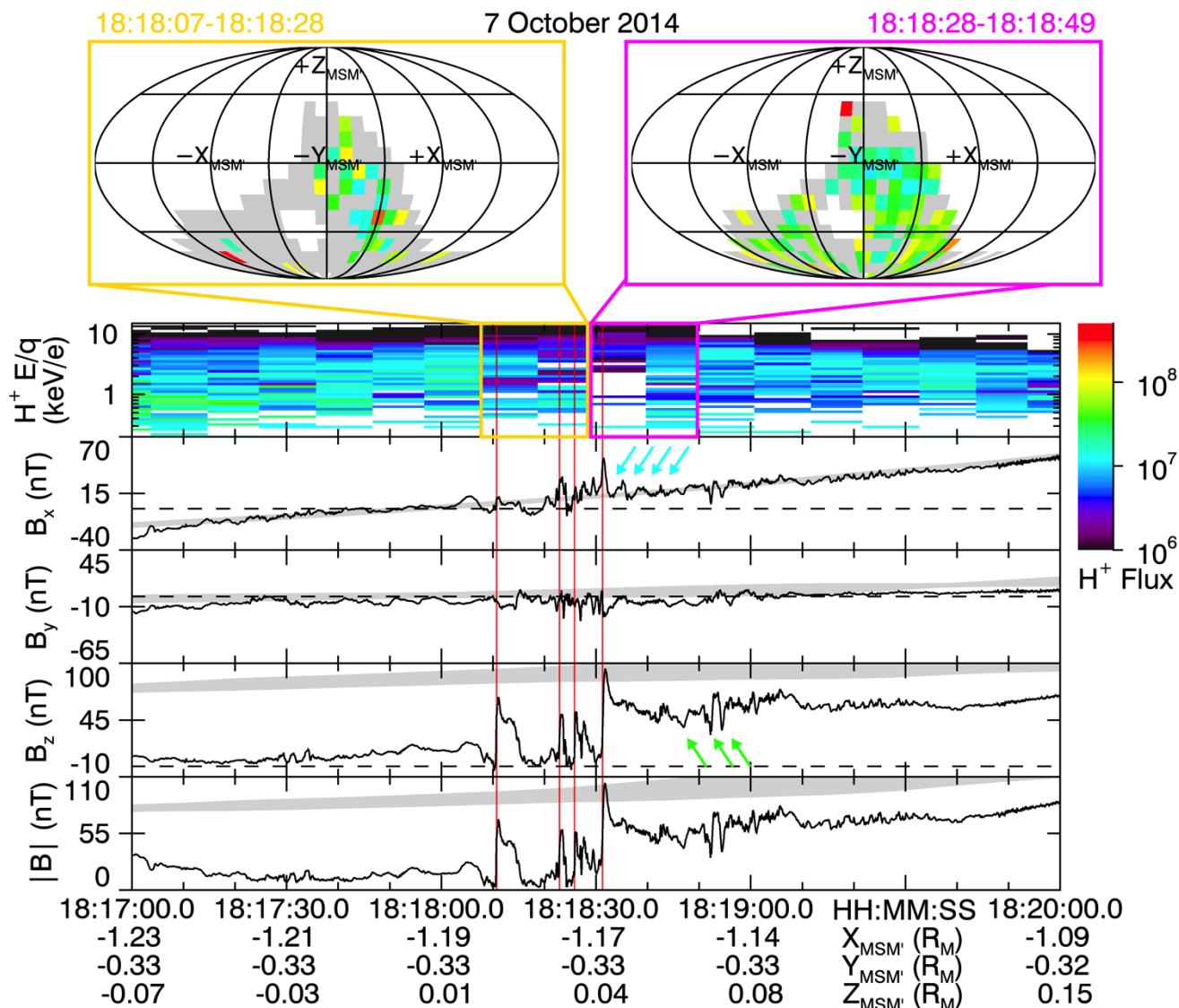


Figure 7. (a) Distribution of the number of dipolarizations observed per orbit versus the median time between dipolarizations during that orbit, where the color bar indicates the number of occurrences. White indicates no occurrences. (b) The marginal distribution of the number of dipolarizations per orbit. (c) The distribution of the time between successive dipolarization fronts. The dashed red lines correspond to thresholds discussed in the text. Arrows in (a) and (c) indicate the number of orbits and dipolarizations, respectively, beyond the range of the plot.

3.4 Flow braking and flux pile-up example

Thus far, our investigation into flow braking and flux pileup at Mercury has been statistical in focus. To ground these statistical results, we conclude this section by presenting an example of flow braking and flux pileup in Mercury’s magnetotail, demonstrating that the statistical results described above are representative of Mercury’s magnetosphere. Figure 8 displays MAG and FIPS observations on 07

575 October 2014 from 18:17:00 to 18:20:00. During this interval, the spacecraft was located in Mercury's
 576 post-midnight magnetotail ($Y_{\text{MSM}'} = -0.33 R_{\text{M}}$) close to Mercury's nightside surface (altitude of ~ 700
 577 km). At these coordinates, we expect the spacecraft to be within the typical braking region identified in
 578 Section 3.1. The spacecraft crossed Mercury's central current sheet, as evidenced by the change in sign
 579 of both B_x and the $Z_{\text{MSM}'}$. During this crossing, MESSENGER encountered several dipolarizations,
 580 marked by vertical red lines, and observed multiple magnetic and plasma signatures of flow braking and
 581 flux pileup.
 582



583 **Figure 8.** FIPS and MAG observations over 18:17:00 to 18:20:00 on 10-07-2014. The panels
 584 from top to bottom are FIPS proton flux (values indicated by the color bar, units of $\text{s}^{-1} \text{cm}^{-2}$), B_x ,
 585 B_y , B_z , and magnetic field strength $|B|$. Below the bottom panel, the time and spacecraft position
 586 are listed. The vertical red lines indicate dipolarization fronts as identified by the selection
 587 algorithm (see Section 2 and Appendix A). The cyan and lime arrows correspond to magnetic
 588 fluctuations described in the text. The grey shaded regions in each magnetic field panel indicate
 589 typical magnetic field conditions at this location in Mercury's magnetotail. In the FIPS proton
 590 flux spectrogram, the gold and magenta boxed scans correspond to the integrated proton flux
 591 maps above the panels. Each flux map indicates the proton flux observed by FIPS as a function
 592 of direction in a Mollweide projection. The color bins correspond to the same color bar (units of
 593

594 $\text{s}^{-1} \text{cm}^{-2} \text{sr}^{-2}$), light grey regions are those within the FIPS field of view but with no observed
595 plasma, and the white regions are those outside the FIPS field of view. Direction labels (e.g.,
596 $+X_{\text{MSM}}$) indicate the direction the protons are travelling towards.
597

598 To provide context to the magnetic field signatures observed during this interval, we include the typical
599 magnetic field conditions at the spacecraft's location as shaded grey regions in each of the magnetic
600 field panels. To determine these conditions, for each point in the magnetic field time series within this
601 interval, we select the 10,000 magnetic field measurements taken closest to the spacecraft's current
602 position that do not belong to the current orbit. We perform a weighted average on these measurements,
603 using the squared distance from each measurement to the current spacecraft position as that
604 measurement's weight, and evaluate variance. These statistical magnetic field conditions not only reflect
605 typical or background observations but also reveal effects of the spacecraft's orbit. For example, the
606 crossing of the central current sheet marked by the reversal in B_x agrees well with the statistical
607 magnetic field description, confirming that this crossing is a result of spacecraft motion rather than
608 current sheet motion.
609

610 Prior to the arrival of the dipolarizations, the northward component of the magnetic field (B_z) is weak at
611 ~ 10 nT. At this location, the spacecraft typically observes $B_z \sim 70$ nT (grey shaded region) indicating
612 that the current sheet is substantially thinned compared to nominal conditions. Each dipolarization
613 increases the northward component and total field strength, however, the first three dipolarizations
614 represent only transient increases (i.e., local plasma sheet thickening). The dipolarization fronts of the
615 first three dipolarizations increase the northward component (ΔB_z) by 68.2 nT, 38.6 nT, and 45.6 nT
616 over a time of 0.75 s, 0.45 s, and 0.45 s, respectively. Although each of these three dipolarizations reach
617 field strengths of ~ 40 -50 nT following their dipolarization fronts, the enhancements are short-lived, with
618 the magnetic field returning to pre-dipolarization values 5.50 s, 1.65 s, and 4.55 s after the start of each
619 dipolarization, respectively. The final, and largest, dipolarization is associated with a prolonged
620 enhancement of the magnetic field. The final dipolarization front increases B_z by 83.4 nT over 0.90 s,
621 reaching the statistically-observed B_z for the only time during this interval. The final dipolarization front
622 reaches a local maximum in B_z (95 nT), but unlike the other dipolarizations, the magnetic field does not
623 return to pre-dipolarization values. Instead, B_z remains enhanced at ~ 55 nT with fluctuations of ± 13 nT
624 through the remainder of the interval. This magnetic field is still weaker than what is normally observed
625 at this location (~ 100 nT) but is notably enhanced above the field at the beginning of the interval,
626 representing a more permanent dipolarization of the field.
627

628 In addition to these B_z signatures, the dipolarizations within this interval are also associated with B_x and
629 B_y perturbations. The first dipolarization is associated with intensification of both B_x and B_y , while the
630 final three dipolarizations display larger-amplitude quasi-periodic fluctuations in both B_x and B_y . These
631 quasi-periodic structures are most readily observed with the third and fourth dipolarizations. Between
632 the third and fourth dipolarizations, the enhancements in B_x last for ~ 1 s over which B_x changes by ~ 13
633 nT. The largest B_x perturbation is associated with the final dipolarization front, with $\Delta B_x = 30$ nT. This
634 large B_x perturbation is associated with a bipolar B_y perturbation, consistent with the structure of an
635 electromagnetic pulse associated with Alfvén waves (e.g., Parks et al., 2007). Following the final
636 dipolarization front, additional fluctuations in B_x and B_y are observed. These perturbations (marked by
637 cyan arrows) are perpendicular to the magnetic field direction, have amplitudes ~ 6 nT, and period ~ 3.5
638 s. Near $\sim 18:18:55$, additional fluctuations are observed in the magnetic field (marked by lime arrows),
639 although these are predominately parallel to the magnetic field (primarily along B_z). These perturbations
640 are similar to those analyzed at higher latitudes by Sun et al. (2015). The perpendicular fluctuations
641 following the final dipolarization front are consistent with Alfvén waves, while the later parallel

642 fluctuations are consistent with compressional wave modes. Following the interpretation of Sun et al.
643 (2015), these waves are suggestive of flow braking.

644
645 To determine if these dipolarizations are associated with bulk plasma flows, we examine FIPS proton
646 flux maps. The two FIPS scans that cover the first three dipolarizations correspond to the gold-boxed
647 flux map, while the scans that cover the final dipolarization correspond to the magenta-boxed flux map.
648 For both ranges, the FIPS field of view is oriented such that it most readily detects protons traveling in $-$
649 Y_{MSM} and $-Z_{\text{MSM}}$ directions. While the missing regions of velocity space are too large to
650 unambiguously determine flow direction and magnitude, the FIPS scans that cover the first three
651 dipolarizations (18:18:07 to 18:18:28) are suggestive of a sunward flow with more plasma traveling in
652 $+X_{\text{MSM}}$ than in $-X_{\text{MSM}}$. In contrast, the final dipolarization does not appear to be associated with a
653 substantial flow, with its flux map (18:18:28 to 18:18:49) appearing substantially more isotropic. The
654 average energy of protons within 45° of $+X_{\text{MSM}}$ is 11.2 ± 4.6 keV in the first distribution and 3.6 ± 1.3
655 keV in the second. In contrast, the average energy of protons along all directions in each distribution is
656 2.8 ± 0.4 keV and 3.2 ± 0.2 keV, respectively. The energy of protons near $+X_{\text{MSM}}$ decreases from much
657 greater than the distribution-average energy in the first distribution to within uncertainty of it within the
658 second distribution, consistent with the deceleration of a sunward flow.

659
660 Taken together, these magnetic field and plasma observations are indicative of flow braking and flux
661 pileup in Mercury's magnetotail. In the span of ~ 30 s, the spacecraft observed four dipolarizations. The
662 first three appear associated with sunward flow and pass over the spacecraft, resulting in temporary,
663 transient increases in the magnetic field. The final dipolarization, in contrast, displays no meaningful
664 flow along X_{MSM} , and is instead associated with a prolonged magnetic field enhancement, characteristic
665 of flow braking and flux pileup. Additionally, perturbations in the magnetic field following the final
666 dipolarization are consistent with Alfvén and compressional waves expected to be associated with flow
667 braking at Mercury (Sun et al., 2015). From the first dipolarization to the last in this time series, the
668 spacecraft moved only 40 km sunward, 3 km duskward, and 60 km northward. For the spacecraft to
669 observe a series of sunward-traveling dipolarizations followed by an approximately stagnant flux pileup
670 region while moving only a small distance in Mercury's magnetotail, it is possible that the final
671 dipolarization may in fact be the piled-up signature of the first three dipolarizations after they
672 experienced intense flow braking.

673 674 **4. Discussion**

675
676 Using an algorithm to identify magnetotail dipolarizations in the magnetic field time series, we have
677 presented both statistical and case study evidence for the flow braking and subsequent magnetic flux
678 pileup associated with dipolarizations in Mercury's magnetotail. We find that downtail of the braking
679 region, the frequency of dipolarizations and the typical sunward flow speed of these structures remains
680 approximately constant. As dipolarizations approach Mercury's near-tail region, as indicated by where
681 the proton plasma beta (β) reaches unity, both the frequency and flow speed of dipolarizations decrease
682 substantially. These observations are analogous to the earliest evidence for the existence of a flow-
683 braking region at Earth (e.g., Shiokawa et al., 1997). While Mercury's braking region is thinner (~ 500
684 km) and situated closer to the planet (~ 900 km in altitude) than Earth's, the intense magnetic pressure
685 gradients at both planets appear responsible for flow braking and deflection. Coincident with the
686 decrease in dipolarization frequency and flow speed, the magnetic pressure gradient in Mercury's near-
687 tail region increases by a factor of 60 ± 20 . The proton plasma pressure gradient also increases at this
688 location, but it increases by a more modest factor (16 ± 7).

689

690 We find that as these dipolarization flows brake, they accumulate magnetic flux in Mercury's near-tail
691 region. Within the braking region, dipolarizations are associated with prolonged enhancements in the
692 magnetic field, as opposed to transient enhancements observed with dipolarizations traveling quickly
693 over the spacecraft upstream of the braking region. We examine the magnetic flux budget of both this
694 pileup region and of individual dipolarizations to determine that spacecraft observations support these
695 statistical findings. Indeed, although building the synoptic flux pileup signature requires several
696 dipolarizations (5 ± 2), dipolarizations are typically observed in series, such that the spacecraft has
697 observed this number or more of dipolarizations in sequence. More simply, we estimate that the flux
698 pileup region contains 0.28 ± 0.08 MWb. Loading of Mercury's magnetotail increases the magnetic flux
699 content of the lobes by 0.69 ± 0.38 MWb (Imber & Slavin, 2017), so there is sufficient magnetic flux
700 loaded into the magnetotail during a typical substorm at Mercury to develop the flux pileup region (i.e.,
701 large-scale dipolarization).
702

703 4.1 Westward expansion of magnetic flux pileup 704

705 We find that the synoptic signature of magnetic flux pileup associated with dipolarizations in Mercury's
706 magnetotail exhibits an asymmetry about local midnight, with a stronger dipolarized field pre-midnight
707 than post-midnight. This asymmetry in pileup is likely related to the asymmetry in dipolarization
708 occurrence and westward expansion of the pileup region. Consistent with previous studies of Mercury's
709 dipolarizations (Sun et al., 2016; Dewey et al., 2018), we find that dipolarizations are more common to
710 Mercury's post-midnight magnetotail as measured both by frequency and by fraction of orbits that
711 possess them. Without the ability to constrain the magnetic flux transported by each dipolarization
712 independently, we interpret the increased rate of dipolarizations post-midnight to indicate that more
713 magnetic flux is usually transported to the post-midnight inner magnetosphere than that pre-midnight,
714 such that we expect pileup to initiate more commonly post-midnight. If pileup is usually initiated in the
715 post-midnight sector, then its expansion westward into the pre-midnight sector may be responsible for
716 the statistical pileup signature we observe there. In Figure 3b, the average V_y flow of bins that intersect
717 the $\beta = 1$ contour or are planetward of it is 53 ± 31 km/s, consistent with westward motion about the
718 planet. Westward expansion may explain why there are instances of pileup observed pre-midnight but it
719 does not immediately explain why the statistical pre-midnight pileup signature is stronger than that post-
720 midnight.
721

722 We hypothesize that two factors may contribute to the pileup strength asymmetry. For bins within the
723 breaking region in Figure 5a, we observe that the post-midnight bins contain a greater average number
724 of dipolarizations (44 ± 7) than the pre-midnight bins (17 ± 5). Similarly, the standard error in δB_z is
725 greater post-midnight (5.0 ± 0.9 nT) compared to pre-midnight (2.8 ± 0.5 nT). We interpret the larger
726 number of dipolarizations and the greater variance in the pileup signature post-midnight to indicate that
727 the post-midnight statistical pileup signature may be averaged down by weak or non-instances of pileup.
728 One explanation could be that there is a threshold of pileup above which flux expands pre-midnight. At
729 Earth, azimuthal expansion occurs after substantial pileup. If this is true for Mercury, then while pileup
730 of all strengths may be observed post-midnight, only sufficiently strong instances of pileup expand
731 westward and can be observed pre-midnight. In other words, weaker instances of pileup act to dilute the
732 statistical post-midnight pileup signature. A second and similar explanation could be that some
733 dipolarizations within the typical breaking region may not have experienced strong breaking when they
734 are observed by the spacecraft. Such dipolarizations are not expected to produce a pileup signature, so
735 when they are observed in the braking region, they would weaken the statistical pileup signature there.
736 For example, the case study examined in Section 3.4 contains four dipolarizations, only the last of which
737 exhibits pileup. The four dipolarizations map to the same bin in Figure 5a so the first three
738 dipolarizations dilute the pileup signature of the fourth. These two factors have different physical

739 mechanisms but the same implication: the pre-midnight pileup signature is biased by stronger, less
740 frequent instances of pileup resulting from westward expansion while the post-midnight signature is
741 averaged down by weak or non-pileup events. Future investigations into this topic at Mercury will be of
742 particular value in addressing the degree to which these mechanisms explain the asymmetry in pileup.

743

744 **4.2 Substorm current wedge formation**

745

746 At Earth, flux pileup is associated with the substorm current wedge: could a current wedge exist at
747 Mercury? Without ground magnetometers or multi-point spacecraft observations, it may be difficult to
748 determine unambiguously. However, the results described in Section 3 suggest it may be possible, if not
749 common, to Mercury's substorms. Alfvén waves, and the field-aligned currents they carry, communicate
750 motion of magnetic field lines of the magnetosphere to the inner conducting boundary in which they are
751 rooted (Southwood & Kivelson, 1991). For Earth, this boundary is the ionosphere, while at Mercury, it
752 is its large conducting core. For a static field-aligned current system like the substorm current wedge to
753 establish, it requires multiple bounces of the current-carrying Alfvén waves (see, e.g., Kepko et al.,
754 2015b). At Mercury's braking region, we find a typical Alfvén speed of $\sim 1,000$ km/s (see Figure 4d).
755 We estimate, by assuming dipole field line geometry, that field lines are $\sim 2 R_M$ in length above
756 Mercury's conducting core at local midnight within the braking region. For such locations close to the
757 planet, the assumption of dipole field line geometry is expected to be valid (see, e.g., Rong et al., 2018).
758 To execute a complete round-trip bounce would therefore require ~ 10 s for an Alfvén wave assuming
759 the Alfvén speed remains constant along the field line. If we assume the magnetic field strength along
760 the field line scales like that of a dipole field line, then the round-trip time would be ~ 6 s. The typical
761 substorm unloading time at Mercury is ~ 100 s (Imber & Slavin, 2017), allowing for many bounces of
762 Alfvén waves within the braking region.

763

764 Although the typical substorm unloading duration allows for many (~ 10 - 16) bounces of Alfvén waves to
765 attempt to establish a static current system, the resistive regolith that covers Mercury's conductive core
766 presents additional restraints on establishing a current wedge. To communicate with the core, the skin
767 depth of the Alfvén wave must be greater than the depth of the regolith. With a period of ~ 6 - 10 s and a
768 height-integrated regolith conductivity of ~ 1 siemen (Anderson et al., 2014), the skin depth of these
769 Alfvén waves would be between 750-960 km, which is greater than the regolith layer (~ 400 km). While
770 these Alfvén waves reach the conductive core, their passage through the resistive regolith reduces their
771 current density. In a round-trip bounce, the waves pass through an accumulated $\sim 1,600$ km of regolith,
772 such that the amplitude (i.e., current density) of the waves after a complete bounce would only be ~ 12 -
773 19% the initial value. Therefore, while a single Alfvén wave within the braking region may complete a
774 sufficient number of bounces during a typical substorm unloading to establish a static field-aligned
775 current system, the resulting current density would be negligible. Furthermore, while the bounce time is
776 substantially smaller than the substorm unloading time at Mercury, it is on the similar time scale as an
777 individual dipolarization. As observed by dipolarizations passing over the spacecraft, the transient
778 increase in the magnetic field associated with individual dipolarizations last for ~ 10 s (see Dewey et al.,
779 2017 and Figure 5b above). Dipolarizations are expected to interact with the braking region for about
780 this duration as well. This timescale allows for only ~ 1 - 2 round-trip bounces of an Alfvén wave, an
781 insufficient number to prevent the dipolarization structure from dissipating. Both the damping of Alfvén
782 waves and the dissipation of an individual dipolarization structure before a static field-aligned system
783 can be established point towards a common solution: continuous supply of dipolarizations.

784

785 When observed, dipolarizations are more commonly observed in series with other dipolarizations than as
786 isolated events (see Figure 7b). A series of dipolarizations, one after another, would supply new Alfvén
787 waves to the braking region (e.g., Sun et al., 2015 and Section 3.4 above) and allow existing Alfvén

788 waves to maintain the magnetic shear about incoming dipolarizations that separate them from the
789 surrounding plasma (i.e., prevent dissipation). Indeed, from flux budget analysis of a typical
790 dipolarization compared with the flux loaded into the magnetotail (Imber & Slavin, 2017), we expect
791 multiple (13 ± 9) dipolarizations during a substorm unloading phase. With most dipolarizations observed
792 ~ 5 -20 s apart (Figure 7c), these dipolarizations would arrive at the braking region within 1-2 Alfvén
793 bounce times of another. Therefore, despite the limitations imposed by the conducting core, the resistive
794 regolith, and the Alfvén bounce times, observations of dipolarizations at Mercury suggest a current
795 wedge structure appears possible to form in Mercury’s magnetotail. With the expectation that such a
796 current wedge at Mercury would require the interaction between the field-aligned current systems (i.e.,
797 Alfvén waves) of multiple, successive dipolarizations, it is surprisingly similar to the “wedgelet”
798 conceptual model of Earth’s substorm current wedge.
799

800 With the formation of a current wedge possible at Mercury, we determine its characteristics by
801 examining the synoptic flux pileup signature (i.e., large-scale dipolarization) of Figure 5. Using a simple
802 current wedge line model (e.g., Poh et al., 2017b), we estimate that the current consistent with this
803 enhanced δB_z would need to be $\sim 14.6 \pm 5.0$ kA in the plasma sheet. This current is ~ 20 times weaker
804 than that at Earth (e.g., Kepko et al., 2015b; Birn et al., 2019). From the weak sunward flow in the
805 braking region (~ 50 -100 km/s), we estimate that the potential drop across the current wedge in the
806 equatorial plane would be $\sim 12.2 \pm 3.4$ kV, indicating a height-integrated electrical conductance of ~ 0.8
807 ± 0.4 siemens, which is consistent with recent estimates from Mercury’s Region-1 static current system
808 (Anderson et al., 2014).
809

810 **4.3 Core induction and surface precipitation**

811
812 The substorm current wedge may not be the only means by which dipolarizations and the magnetotail
813 couple to Mercury’s conducting core. Mercury’s core responds to compression of the magnetosphere by
814 inducing currents on its surface to resist these changes. The topic of induction has been most thoroughly
815 studied with regards to changes in solar wind dynamic pressure (e.g., Slavin et al., 2014; Jia et al., 2015;
816 Zhong et al., 2015; Johnson et al., 2016; Jia et al., 2019) but studies of Mercury’s magnetotail have also
817 discussed the possibility of inducing currents on the core’s nightside surface in response to compression
818 of the planet’s nightside inner magnetosphere (e.g., Dewey et al., 2018). Based on our findings, we
819 expect that dipolarizations are unlikely to elicit a strong inductive response from the planetary core.
820 Dipolarizations provide only small increases in dynamic pressure with which to compress Mercury’s
821 nightside magnetic field. Given the characteristics of dipolarizations described in Section 3 and by
822 Dewey et al. (2018), the typical dynamic pressure of a dipolarization is of order ~ 0.1 nPa. Mercury’s
823 inner magnetosphere has magnetic pressure of order ~ 5 nPa (see Figure 4) so individual dipolarizations
824 are unlikely to substantially compress the nightside inner magnetosphere and generate inductive currents
825 on the core. By comparison, changes in solar wind dynamic pressure along Mercury’s highly eccentric
826 orbit (~ 11 nPa at aphelion to ~ 26 nPa at perihelion, Slavin & Holzer, 1981) result in induction currents
827 that change Mercury’s magnetic moment by only $\sim 5\%$ (Johnson et al., 2016). To reach similar dynamic
828 pressures in Mercury’s magnetotail, dipolarizations would need to be associated with extreme density ($>$
829 5 cm^{-3}) and flow speeds ($> 1,000$ km/s). Even then, dipolarizations are localized in cross-tail extent so
830 they would only compress the nightside inner magnetosphere regionally. Increases in solar wind
831 dynamic pressure compress the dayside magnetosphere globally so any nightside inductive currents
832 would be much smaller in spatial extent on the core than the dayside equivalents.
833

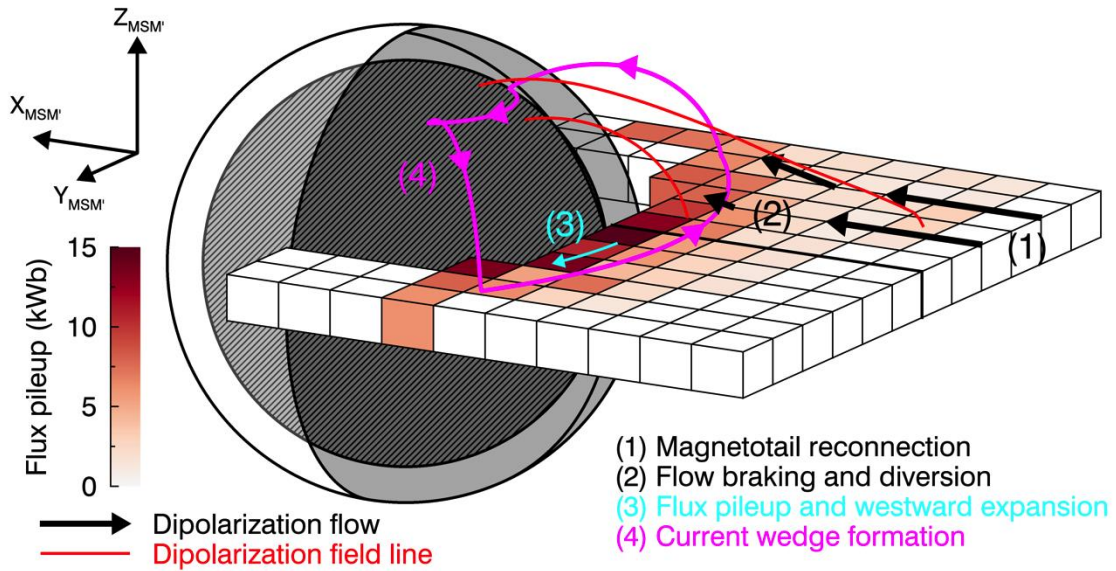
834 Dipolarizations also interact with Mercury’s surface. There is some evidence that a small fraction of
835 dipolarizations may reach Mercury’s low latitude nightside surface. The occurrence maps of
836 dipolarizations (Figure 2) indicate that some dipolarizations are observed at < 200 km altitude.

837 Furthermore, organizing dipolarization frequency about $\beta = 1$ (Figure 4) indicates that far downstream
838 of the braking region (e.g., $\Delta X_{\text{MSM}} = 0.5 R_M$) dipolarizations are still observed even if at a low rate. At
839 these locations, the rate of dipolarizations ($\sim 0.1\text{-}0.2 \text{ min}^{-1}$) is much lower than the downtail occurrence
840 ($\sim 0.6 \text{ min}^{-1}$) implying that no more than $\sim 10\text{-}20\%$ of dipolarizations travel far beyond the braking
841 region. At the flanks of the magnetotail, dipolarizations traveling this far beyond $\beta = 1$ may return their
842 magnetic flux to the dayside directly, while those behind the planet may impact the low latitude surface
843 (or approach within a gyroradius of the surface). As most precipitation in Mercury's plasma sheet is
844 expected at mid- or high-latitudes (e.g., Korth et al., 2014), the opportunity for dipolarizations to
845 transport plasma and magnetic flux directly to the low latitude surface may have consequences for
846 exospheric generation and space weathering (e.g., Raines et al., 2016). Aside from dipolarizations
847 reaching the low-latitude nightside surface, the close proximity of the braking region to the planet's
848 surface (altitude of $\sim 900 \text{ km}$) results in large expected loss cones ($\sim 25\text{-}40^\circ$) such that substantial plasma
849 precipitation may occur with most dipolarizations in the braking region already. The mass transport of
850 dipolarizations in Mercury's magnetotail deserves further dedicated study.

851 852 **5. Conclusions**

853
854 We present strong evidence for flow braking and magnetic flux pileup associated with dipolarizations in
855 Mercury's magnetotail. We summarize our findings in Figure 9, a schematic representation of flow
856 braking, flux pileup, and current wedge formation. Dipolarizations first begin in the mid-tail as a product
857 of reconnection and are transported sunward by the fast reconnection outflows. As dipolarizations and
858 their associated flows approach Mercury's inner magnetosphere, the flows encounter steep magnetic
859 pressure gradients from Mercury's planetary dipole field, causing the flows to brake and deflect. A small
860 fraction (no more than $\sim 10\text{-}20\%$) of dipolarizations may be able to reach the dayside magnetosphere or
861 Mercury's nightside surface while the remainder typically brake within a region $\sim 500 \text{ km}$ in thickness
862 located $\sim 900 \text{ km}$ in altitude above Mercury's local midnight surface as evidenced by substantial and
863 significant decreases in dipolarization frequency and sunward flow speed. As dipolarizations brake, their
864 transported magnetic flux accumulates. Current-carrying Alfvén waves generated by the motion and
865 braking of the dipolarization field lines communicate these changes to Mercury's conductive core. As
866 additional dipolarizations brake and pileup, the large-scale dipolarization near the inner magnetosphere
867 expands westward into the pre-midnight magnetotail. Simultaneously, the interaction of the Alfvén
868 waves from the braking of multiple, continuous dipolarizations may be able to establish a large-scale
869 current system to support the enhanced magnetic field within the pileup region, akin to Earth's substorm
870 current wedge. Despite the differences between Mercury and Earth's magnetospheres, namely the
871 smaller spatiotemporal scales, enhanced effects of magnetic reconnection, and lack of ionosphere at
872 Mercury, the dynamics of dipolarizations are surprisingly similar. While we have presented both
873 statistical analysis and a case study in support of our conclusions, observations from the en route
874 BepiColombo spacecraft mission and global modeling simulations of Mercury's magnetosphere will be
875 of particular value to continue to investigate and constrain these results.

876



877
878 **Figure 9.** Schematic of flow braking, flux pileup, and current wedge formation from
879 dipolarizations within Mercury's magnetotail. The colored boxes are the pileup observations
880 from Figure 5. Features are at accurate scaling with respect to each other.
881

882 **Acknowledgements**
883

884 NASA's Earth and Space Science Fellowship Program (80NSSC17K0493) supported R. M. Dewey.
885 NASA Grants NNX16AJ67G and 80NSSC18K1137 supported W. Sun and J. A. Slavin. NASA
886 Discovery Data Analysis Grant NNX16AJ05G supported J. M. Raines. A. R. Azari was supported by
887 the National Science Foundation Graduate Research Fellowship Program under Grant No. DGE
888 1256260. R. M. Dewey would like to thank A. Runov, A. Artemyev, C. Gabrielse, V. Angelopoulos,
889 and T. Nishimura for valuable conversations. All MESSENGER data used in this study are available
890 from the NASA Planetary Data System at <https://pds-ppi.igpp.ucla.edu/search/?sc=Messenger>
891

892 Appendix A: Dipolarization identification algorithm

893

894 The dipolarization identification technique is described briefly in Section 2. In this appendix, we
 895 describe the procedure in greater detail. Previous approaches to determining dipolarizations via
 896 autonomous algorithms have focused on identifying the leading edge of the event (dipolarization front)
 897 using a sliding window (e.g., Liu et al., 2013; Sun et al., 2016). We follow a similar, but modified
 898 approach, first identifying potential dipolarization fronts within the magnetic field time series and then
 899 applying a series of physical tests to determine if these signals represent dipolarizations. We take
 900 advantage of the initial statistical characterization of dipolarizations at Mercury from Sundberg et al.
 901 (2012), Sun et al. (2016), and Dewey et al. (2017) to set several empirical limits in identifying events.

902

903 To identify potential dipolarization fronts, we examine each point in the $B_z(t)$ time series for a strong,
 904 local, coherent, positive gradient. At point i in the time series (i.e., $t = t_i$), we determine the minimum
 905 time (Δt) by which B_z increases by ΔB_z , i.e., $B_z(t_i + \Delta t) = B_z(t_i) + \Delta B_z$. The parameter ΔB_z will
 906 therefore be the minimum increase in B_z of an identified dipolarization front. We use $\Delta B_z = 10$ nT,
 907 which corresponds the 5th percentile of dipolarization front ΔB_z identified by Dewey et al. (2017). In
 908 other words, 95% of dipolarizations identified by Dewey et al. (2017) have dipolarization front $\Delta B_z >$
 909 10 nT. For the interval of t_i to $t_i + \Delta t$ to qualify as a potential dipolarization front, we require:

910

- 911 1. $\Delta B_z / \Delta t \geq 5$ nT/s;
- 912 2. $\text{minimum}(B_z(t_i < t < t_i + \Delta t)) \geq B_z(t_i)$; and
- 913 3. $\mu(\delta B_z(t_i < t < t_i + \Delta t)) > \sigma(\delta B_z(t_i < t < t_i + \Delta t))$

914

915 where $\delta B_z(t)$ is the point-to-point change in $B_z(t)$, μ is the mean function, and σ is the standard
 916 deviation function. The first criterion requires local gradients to be both strong and positive, while the
 917 last two criteria require local gradients to be coherent. We set the threshold of the first criterion
 918 empirically by examining dipolarizations of Dewey et al. (2017), the distribution of $\Delta B_z(\Delta t)$ across the
 919 1,946 dipolarization-search intervals, and to avoid misinterpreting the spacecraft's motion through the
 920 current sheet (or the current sheet's motion over the spacecraft) as a potential event. Each group of
 921 sequential points in the time series that meet these three criteria is determined to be potential
 922 dipolarization front. We require that each potential dipolarization front have a minimum duration of 0.4
 923 s (eight or more sequential MAG observations) to ensure the dipolarization front is well resolved. For
 924 comparison, Dewey et al. (2017) found a minimum dipolarization front duration of 0.7 s.

925

926 To determine if a potential dipolarization front corresponds to a dipolarization or not, a series of tests are
 927 applied. These tests include physical and statistical considerations and are designed to mimic signals that
 928 one's eye would use to select dipolarizations and to avoid false-positives from other magnetotail
 929 phenomena, such as flux ropes, tail flapping, and magnetospheric waves. Because the duration of
 930 dipolarization fronts can vary substantially (i.e., from < 1 s to > 5 s, see Dewey et al., 2017), these tests
 931 use time durations standardized by the potential dipolarization front's duration Δt_{DF} . The first test
 932 evaluates if the increase in B_z across the potential dipolarization front is meaningful compared to the
 933 fluctuations in the magnetic field that surround it:

934

$$935 \frac{\mu(B_z(t_2 < t < t_2 + \gamma \Delta t_{DF})) - \mu(B_z(t_1 - \alpha \Delta t_{DF} < t < t_1))}{\sqrt{\sigma(B_z(t_2 < t < t_2 + \gamma \Delta t_{DF}))^2 + \sigma(B_z(t_1 - \alpha \Delta t_{DF} < t < t_1))^2}} > \eta$$

936

937 where t_1 is the start time of the potential dipolarization front, t_2 is the end time of the potential
 938 dipolarization front, and therefore $\Delta t_{DF} = t_2 - t_1$. The parameters α , γ , and η are determined from
 939 optimization, described below. The second test evaluates if the potential dipolarization has sufficient
 940 duration:

$$941 \quad \tau_2 > \varepsilon \Delta t_{DF}$$

942 where

$$943 \quad \tau_2 = t(B_z = \tilde{\mu}(B_z(t_1 < t < t_2)); t > t_2) - t_2$$

944

945 and $\tilde{\mu}$ is the median function. The parameter τ_2 reflects the duration of time following the end of the
 946 potential dipolarization front that B_z is elevated above the median B_z during the potential front. The
 947 parameter ε is determined from optimization. The third test evaluates if the potential dipolarization
 948 stands above the preceding magnetic field for sufficient time:

949

$$950 \quad t_1 - t_0 - \tau_2 > \zeta \Delta t_{DF}$$

951 where

952

$$\int_{t_0}^{t_1} \lambda(t) dt = \tau_2$$

953 and

954

$$\lambda(t) = \begin{cases} 1 & \text{for } B_z(t) \geq \tilde{\mu}(B_z(t_1 < t < t_2)) \\ 0 & \text{for } B_z(t) < \tilde{\mu}(B_z(t_1 < t < t_2)) \end{cases}$$

955

956 and ζ is determined from optimization. This third test is similar to the second in that it determines the
 957 duration of time before the potential dipolarization front that the magnetic field was below the median
 958 level during the potential front, but with the addition that it allows for short intervals of time (relative to
 959 the duration of the potential dipolarization) that the field was above the median level. We find that
 960 dipolarizations often occur in series with other dipolarizations (e.g., see Figure 7 within Section 3.3 or
 961 Figure 2 of Sundberg et al., 2012) and that without allowing for an interval of B_z greater than the median
 962 level, many dipolarizations in series would be disqualified. The final test evaluates how the change in B_z
 963 across the dipolarization front compares in magnitude to the preceding field:

964

965

$$\frac{B_z(t_2) - B_z(t_1)}{\mu(B_z(t_1 - \zeta \Delta t_{DF} < t < t_1))} > \nu$$

966

967 where ν is determined by optimization. We experimented with additional tests and tests with different
 968 functional forms, and found that these four tests provide the minimum yet sufficient criteria to determine
 969 which potential dipolarization fronts indeed correspond to dipolarizations.

970

971 To optimize the six (α , γ , η , ε , ζ , and ν) free parameters, we developed a training set of dipolarizations
 972 to determine algorithm performance. We selected, at random, 196 of the 1,946 intervals (~10%) and for
 973 each potential dipolarization front within these selected intervals, evaluated by eye whether it
 974 corresponds to a dipolarization. The 196 intervals contain 1,775 potential dipolarization fronts, of which
 975 623 correspond to dipolarizations and 1,152 do not. By systematically varying the six free parameters,
 976 we evaluated algorithm performance on this training set. We follow the optimization technique outlined
 977 by Azari et al. (2018), which focuses on the Heidke Skill Score (HSS) for evaluating and optimizing
 978 algorithm performance. HSS ranges from $-\infty$ (perfect anti-prediction) to 1 (perfect prediction), with
 979 HSS = 0 representing prediction as good as random change. For a discussion of the advantages of using
 980 HSS for identification algorithms in space physics, see Azari et al. (2018) and references therein. For

981 our algorithm, maximizing HSS to determine free parameter values led to a large fraction of false
982 positives identified as events. At the maximum HSS (0.806), 13.0% of events identified by the algorithm
983 to be dipolarizations were false positives, and 7.1% of all 1,152 non-dipolarizations were detected as
984 events. We therefore modified the Azari et al. (2018) approach by limiting the maximum fraction of
985 false positives to 5%. Setting this limit, the maximum qualifying HSS is 0.764, corresponding to free
986 parameter values of

$$987 \quad \alpha = 1.75$$

$$988 \quad \gamma = 1.50$$

$$989 \quad \eta = 1.75$$

$$990 \quad \varepsilon = 1$$

$$991 \quad \zeta = 2$$

$$992 \quad \nu = 0.3$$

993
994 With these parameters, the rate of dipolarization detection is 73.7%, the rate of non-dipolarizations
995 being detected as events is 2.1%, and the fraction of algorithm-identified events that are false positives is
996 5.0%. The HSS of 0.76 indicates this algorithm identifies dipolarizations much better than random
997 chance. For comparison, semi-autonomous identification of injection events at Saturn by Azari et al.
998 (2018) has an HSS of 0.56, while space weather models typically have $HSS < 0.5$ for predicting
999 magnetic perturbations at ground magnetometer stations (Pulkkinen et al., 2013).

1000

Appendix B: Statistical flows from partial FIPS composite velocity space distributions

To estimate ion bulk flows, we follow the procedure developed by Dewey et al. (2018). We refer readers to that study for technical details of the method and its implementation. Below we present a summary of the method and expand its capabilities to evaluate flows from velocity space distributions less complete than those presented in Dewey et al. (2018).

FIPS cannot measure complete velocity space distributions at its native time resolution due to limitations imposed by the MESSENGER spacecraft. The spacecraft is three-axis stabilized so FIPS only observes $\sim 1.15\pi$ sr of the sky during a single scan. Although the spacecraft does not spin, it does rotate slowly over the course of its orbit (~ 0.04 deg/s) to keep the sunshade pointed sunward and to regulate the pointing of remote sensing instruments. This rotation is too slow for FIPS to construct complete velocity space distributions between subsequent scans but it does change the pointing of the FIPS instrument over time. Constructing a complete velocity space distribution therefore requires combining FIPS scans from different intervals. Selecting FIPS observations of similar magnetospheric phenomena (e.g., dipolarizations) allows us to construct a statistical description of velocity space associated with those events from which we can determine bulk flows.

Despite the number of FIPS scans combined to form a composite velocity space distribution, this distribution will not be complete in velocity space. The center of FIPS's field of view (FOV) is approximately perpendicular to the spacecraft's sunshade so FIPS cannot observe to within $\sim 20^\circ$ of the spacecraft's sunshade axis. The requirement that the sunshade points sunward therefore prevents FIPS from observing within $\sim 20^\circ$ of $\pm X_{\text{MSM}}$. When calculating statistical flows, Dewey et al. (2018) mitigate the effects of missing velocity space regions by comparing the velocity space distribution to that produced by a software model of the FIPS instrument (Dewey, Raines, & Tracy, 2017). In our study, we use fewer FIPS scans on average in constructing composite velocity space distributions, and as a consequence, many of these distributions have larger missing regions than the distributions discussed in Dewey et al. (2018). Figure B1 provides examples of distributions used in determining statistical flows for Figure 3. Figure B1a is a nearly complete distribution similar to that of Dewey et al. (2018) while B1b is less complete.

To determine which velocity components can be reliably determined from these less complete distributions, we define several parameters that quantify how much of velocity space is observed and how symmetric that coverage is. First, we define the FOV distribution $\mathcal{F}(\theta, \phi)$. This distribution has standard spherical coordinates with θ as the zenith angle and ϕ as the azimuth angle. The value of $\mathcal{F}(\theta, \phi)$ is binary: $\mathcal{F}(\theta, \phi) = 1$ for velocity space directions observed by one or more FIPS scans and $\mathcal{F}(\theta, \phi) = 0$ for unobserved directions. We use $\mathcal{F}(\theta, \phi)$ to define the normalized effective steradians Ω_i that can contribute to calculating each velocity component:

$$\Omega_i = \frac{1}{2\pi} \int_0^{2\pi} \int_0^\pi \mathcal{F}(\theta, \phi) |J_i(\theta, \phi)| \sin \theta \, d\theta d\phi$$

where i is a direction (e.g., X_{MSM}) and $J_i(\theta, \phi)$ is the expression of unit vector \hat{i} in spherical coordinates (e.g., $J_x(\theta, \phi) = \sin \theta \cos \phi$). The parameter Ω_i has the range $[0, 1]$ and communicates the weight of the missing regions in determining the velocity component V_i . If $\Omega_i \sim 1$ then any unobserved directions in the composite distribution have little or no effect in determining V_i . Conversely, $\Omega_i \sim 0$ indicates that there is little or no information available to determine V_i . It is worth noting that Ω_i of different velocity components are not independent; $\Omega_x \equiv 1$ requires both $\Omega_y = 1$ and $\Omega_z = 1$. For the distribution in

Figure B1a, $\Omega_x = 0.84$, $\Omega_y = 0.96$, and $\Omega_z = 0.98$, i.e., the distribution is practically complete along Y_{MSM} and Z_{MSM} with the missing regions mostly affecting X_{MSM} . Figure B1b is less complete in coverage and has $\Omega_x = 0.44$, $\Omega_y = 0.60$, and $\Omega_z = 0.59$. Finally, we define the symmetry ratio Φ_i :

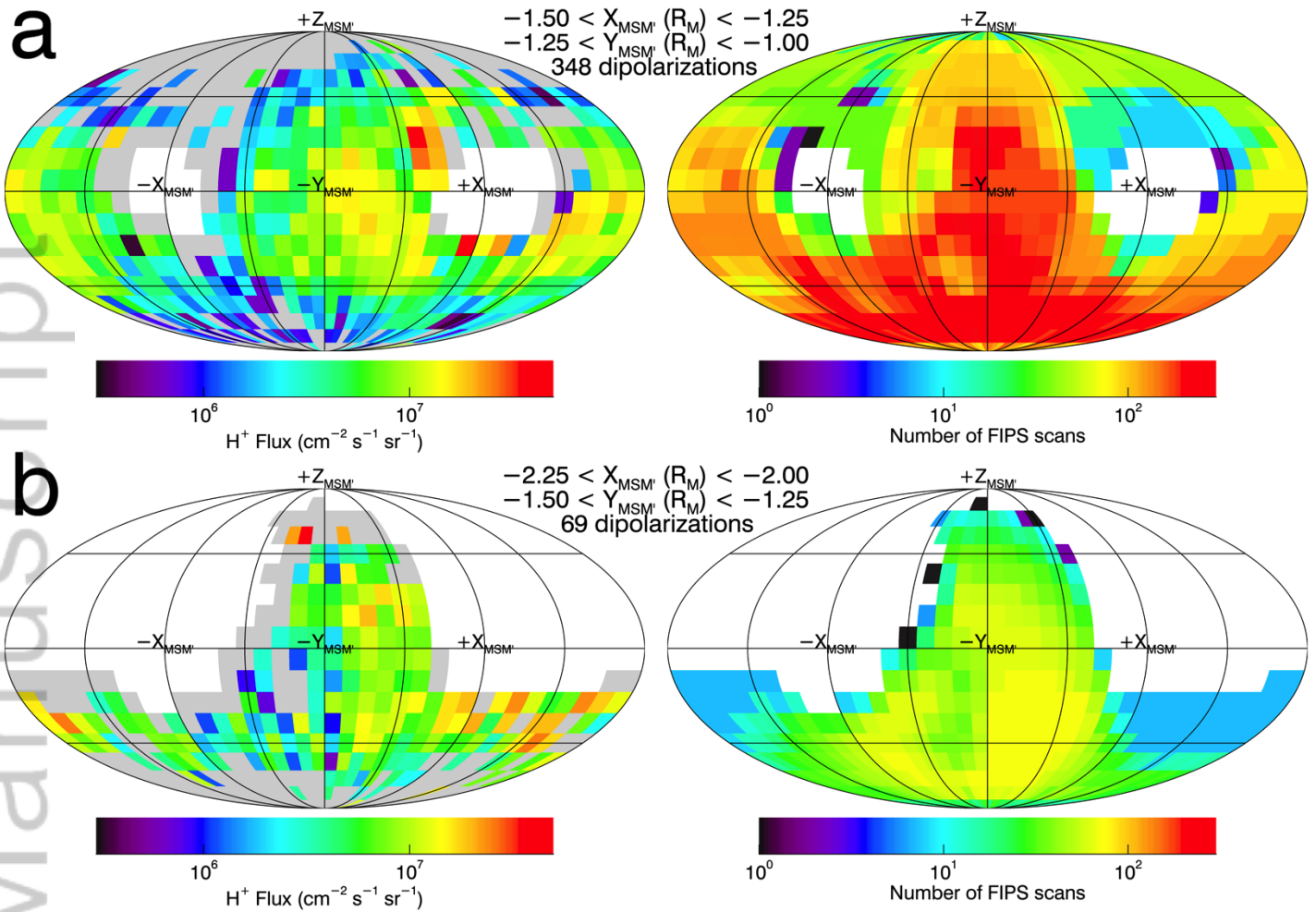
$$\Phi_i = \frac{1 - |\omega_i|}{1 + |\omega_i|}$$

where

$$\omega_i = \frac{1}{2\pi\Omega_i} \int_0^{2\pi} \int_0^\pi \mathcal{F}(\theta, \phi) J_i(\theta, \phi) \sin \theta \, d\theta d\phi$$

is the normalized difference in effective steradians between the $\pm i$ directions. The parameter Φ_i has the range $[(2\Omega_i - 1) > 0, 1]$ and communicates the relative symmetry of Ω_i between the $\pm i$ directions. In other words, $\Phi_i = 1$ indicates that there is no asymmetry in the observed portions of the distribution between $+i$ and $-i$, while $\Phi_i = 0$ indicates that all observed portions of the distribution are in one hemisphere (e.g., only observations of $+i$ and none of $-i$). A $\Phi_i = 0.5$ value indicates that one hemisphere (e.g., $+i$) has twice the observed velocity space contributing to determining V_i than the other hemisphere ($-i$). Figure B1a has $\Phi_x = 0.91$, $\Phi_y = 0.98$, and $\Phi_z = 1.00$, while Figure B1b has $\Phi_x = 0.85$, $\Phi_y = 0.41$, and $\Phi_z = 0.25$. In other words, while there is little or no bias along any direction in Figure B1a, there is substantial asymmetry along $\pm Y_{\text{MSM}}$ and $\pm Z_{\text{MSM}}$ in Figure B1b. Used together, Ω_i and Φ_i indicate how *complete* and *unbiased*, respectively, the velocity space distribution is for determining V_i .

We use the FIPS software model to set thresholds on Ω_i and Φ_i for calculating and displaying velocity components (e.g., Figure 3). With a set of input plasma moments, we use the software model to generate a complete velocity space distribution to which we apply missing angular regions and calculate resulting plasma moments. We generate 12.4 million unique combinations of plasma moments and velocity space coverage to determine how the coverage affects determination of plasma moments. To keep root-mean-squared errors in V_i less than either 25% or 25 km/s (whichever is greater for a given set of plasma moments) requires $\Omega_i > 0.4$ and $\Phi_i > 0.7$. Above these thresholds, errors in proton density are less than 8% or 0.1 cm^{-3} and errors in proton temperature are less than 20% or 2 MK. We implement these thresholds in calculating and displaying statistical plasma flows in Figure 3. If either Ω_i or Φ_i for a given flow component is below its threshold, we do not display that flow component in Figure 3 (i.e., it is displayed as a grey bin). If both Ω_i and Φ_i are above their thresholds, then we display the flow component and incorporate the uncertainty from the missing velocity space regions with the statistical and systematic uncertainties already prescribed by Dewey et al. (2018). For the example distributions in Figure B1, we calculate and display all three flow components from the distribution in Figure B1a, but only calculate and display the V_x component in Figure B1b.



1085
 1086 **Figure B1.** Composite velocity space distributions from FIPS measurements of dipolarizations. (left
 1087 column) Proton flux maps, where white are unobserved regions and grey are observed regions that have
 1088 no measured counts. (right column) Number of FIPS scans that contribute to constructing the proton flux
 1089 maps for each direction in velocity space. White indicates that no scans observe that direction. The text
 1090 between the distributions indicates which location of Figure 3 these distributions correspond to as well
 1091 as the number of dipolarizations used to construct the composite distributions.
 1092

References

- Anderson, B. J., Acuña, M. H., Lohr, D. A., Scheifele, J., Raval, A., Korth, H., & Slavin, J. A. (2007). The Magnetometer instrument on MESSENGER. *Space Science Reviews*, **131**(1-4), 417–450. <https://doi.org/10.1007/s11214-007-9246-7>
- Anderson, B. J., Johnson, C. L., Korth, H., Purucker, M. E., Winslow, R. M., Slavin, J. A., et al. (2011). The global magnetic field of Mercury from MESSENGER orbital observations. *Science*, **333**(6051), 1859–1862. <https://doi.org/10.1126/science.1211001>
- Anderson, B. J., Johnson, C. L., Korth, H., Slavin, J. A., Winslow, R. M., Phillips, R. J., Solomon, S. C., & McNutt Jr., R. L. (2014). Steady-state field-aligned currents at Mercury. *Geophysical Research Letters*, **41**, 7444–7452. <https://doi.org/10.1002/2014GL061677>
- Andrews, G. B., Zurbuchen, T. H., Mauk, B. H., Malcom, H., Fisk, L. A., Gloeckler, G., et al. (2007). The Energetic Particle and Plasma Spectrometer instrument on the MESSENGER spacecraft. *Space Science Reviews*, **131**(1-4), 523–556. <https://doi.org/10.1007/s11214-007-9272-5>
- Angelopoulos, V., Baumjohann, W., Kennel, C. F., Coroniti, F. V., Kivelson, M. G., Pellat, R., et al. (1992). Bursty bulk flows in the inner central plasma sheet. *Journal of Geophysical Research*, **97**(A4), 4027–4039. <https://doi.org/10.1029/91JA02701>
- Ashour-Abdalla, M., El-Alaoui, M., Goldstein, M. L., Zhou, M., Schriver, D., Richard, R., ... Hwang, K.-J. (2011). Observations and simulations of non-local acceleration of electrons in magnetotail magnetic reconnection events. *Nature Physics*, **7**, 360–365. <https://doi.org/10.1038/nphys1903>
- Azari, A. R., Liemohn, M. W., Jia, X., Thomsen, M. F., Mitchell, D. G., Sergis, N., et al. (2018). Interchange injections at Saturn: Statistical survey of energetic H⁺ sudden flux intensifications. *Journal of Geophysical Research: Space Physics*, **123**, 4692–4711. <https://doi.org/10.1029/2018JA025391>
- Baumjohann, W., Hesse, M., Kokubun, S., Mukai, T., Nagai, T., & Petrukovich, A. A. (1999). Substorm dipolarization and recovery. *Journal of Geophysical Research*, **104**, 24995–25000. <https://doi.org/10.1029/1999JA900282>
- Birn, J., Hesse, M., Haerendel, G., Aumjohann, W. B., & Shiokawa, K. (1999). Flow braking and the substorm current wedge. *Journal of Geophysical Research: Space Physics*, **114**(A), 19895–19904.
- Birn, J., Nakamura, R., Panov, E., & Hesse, M. (2011). Bursty bulk flows and dipolarization in MHD simulations of magnetotail reconnection. *Journal of Geophysical Research*, **116**, A01210. <https://doi.org/10.1029/2010JA016083>
- Birn, J., Hesse, M., Nakamura, R., & Zaharia, S. (2013). Particle acceleration in dipolarization events. *Journal of Geophysical Research: Space Physics*, **118**, 1960–1971. <https://doi.org/10.1002/jgra.50132>
- Birn, J., Liu, J., Runov, A., Kepko, L., & Angelopoulos, V. (2019). On the contribution of dipolarizing flux bundles to the substorm current wedge and to flux and energy transport. *Journal of*

1142 *Geophysical Research: Space Physics*, **124**, 5408–5420. <https://doi.org/10.1029/2019JA026658>

1143
1144 Delcourt, D. C., Grimald, S., Leblanc, F., Berthelier, J.-J., Millilo, A., Mura, A., et al. (2003). A
1145 quantitative model of planetary Na⁺ contribution to Mercury's magnetosphere. *Annales*
1146 *Geophysicae*, **21**(8), 1723–1736. <https://doi.org/10.5194/angeo-21-1723-2003>

1147
1148 Delcourt, D. (2013). On the supply of heavy planetary material to the magnetotail of Mercury. *Annales*
1149 *Geophysicae*, **31**(10), 1673–1679. <https://doi.org/10.5194/angeo-31-1673-2013>

1150
1151 Dewey, R. M., Slavin, J. A., Raines, J. M., Baker, D. N., & Lawrence, D. J. (2017). Energetic electron
1152 acceleration and injection during dipolarization events in Mercury's magnetotail. *Journal of*
1153 *Geophysical Research: Space Physics*, **122**, 12,170–12,188.
1154 <https://doi.org/10.1002/2017JA024617>

1155
1156 Dewey, R. M., Raines, J. M., & Tracy, P. J. (2017). Interpreting FIPS density, temperature, and
1157 pressure. NASA Planetary Data System, MESS-E/V/H/SW-EPPS-3-FIPS-DDR-V2.0.

1158
1159 Dewey, R. M., Raines, J. M., Sun, W., Slavin, J. A., & Poh, G. (2018). MESSENGER observations of
1160 fast plasma flows in Mercury's magnetotail. *Geophysical Research Letters*, **45**, 10,110–10,118.
1161 <https://doi.org/10.1029/2018GL079056>

1162
1163 DiBraccio, G. A., Slavin, J. A., Boardsen, S. A., Anderson, B. J., Korth, H., Zurbuchen, T.
1164 H.,...Solomon, S. C. (2013). MESSENGER observations of magnetopause structure and
1165 dynamics at Mercury. *Journal of Geophysical Research: Space Physics*, **118**, 997–1008.
1166 <https://doi.org/10.1002/jgra.50123>

1167
1168 DiBraccio, G. A., Slavin, J. A., Imber, S. M., Gershman, D. J., Raines, J. M., Jackman, C. M., et al.
1169 (2015). MESSENGER observations of flux ropes in Mercury's magnetotail. *Planetary and*
1170 *Space Science*, **115**, 77–89. <https://doi.org/10.1016/j.pss.2014.12.016>

1171
1172 Dubyagin, S., Sergeev, V., Apatenkov, S., Angelopoulos, V., Runov, A., Nakamura, R., ... Larson, D.
1173 (2011). Can flow bursts penetrate into the inner magnetosphere? *Geophysical Research Letters*,
1174 **38**, L08102. <https://doi.org/10.1029/2011GL047016>

1175
1176 Fu, H. S., Cao, J. B., Khotyaintsev, Y. V., Sitnov, M. I., Runov, A., Fu, S. Y., ... Huang, S. Y. (2013).
1177 Dipolarization fronts as a consequence of transient reconnection: In situ evidence. *Geophysical*
1178 *Research Letters*, **40**, 6023–6027. <https://doi.org/10.1002/2013GL058620>

1179
1180 Gabrielse, C., Harris, C., Angelopoulos, V., Artemyev, A., & Runov, A. (2016). The role of localized
1181 inductive electric fields in electron injections around dipolarizing flux bundles. *Journal of*
1182 *Geophysical Research: Space Physics*, **121**, 9560–9585. <https://doi.org/10.1002/2016JA023061>

1183
1184 Gershman, D. J., Slavin, J. A., Raines, J. M., Zurbuchen, T. H., Anderson, B. J., Korth, H.,...Solomon,
1185 S. C. (2013). Magnetic flux pileup and plasma depletion in Mercury's subsolar magnetosheath.
1186 *Journal of Geophysical Research: Space Physics*, **118**, 7181–7199.
1187 <https://doi.org/10.1002/2013JA019244>

1188
1189 Imber, S. M., & Slavin, J. A. (2017). MESSENGER observations of magnetotail loading and unloading:
1190 Implications for substorms at Mercury. *Journal of Geophysical Research: Space Physics*, **122**,

11,402–11,412. <https://doi.org/10.1002/2017JA024332>

Janhunen, P., & Kallio, E. (2004). Surface conductivity of Mercury provides current closure and may affect magnetospheric symmetry. *Annals of Geophysics*, **22**(5), 1829–1837. <https://doi.org/10.5194/angeo-22-1829-2004>

Jia, X., Slavin, J. A., Gombosi, T. I., Daldorff, L. K. S., Toth, G., & van der Holst, B. (2015). Global MHD simulations of Mercury's magnetosphere with coupled planetary interior: Induction effect of the planetary conducting core on the global interaction. *Journal of Geophysical Research: Space Physics*, **120**, 4763–4775. <https://doi.org/10.1002/2015JA021143>

Jia, X., Slavin, J. A., Poh, G., DiBraccio, G. A., Toth, G., Chen, Y., et al. (2019). MESSENGER observations and global simulations of highly compressed magnetosphere events at Mercury. *Journal of Geophysical Research: Space Physics*, **124**, 229–247. <https://doi.org/10.1029/2018JA026166>

Johnson, C. L., Philpott, L. C., Anderson, B. J., Korth, H., Hauck, S. A. II, Heyner, D., et al. (2016). Messenger Observations Of Induced Magnetic Fields In Mercury's Core. *Geophysical Research Letters*, **43**, 2436–2444. <https://doi.org/10.1002/2015GL067370>

Karlsson, T., Hamrin, M., Nilsson, H., Kullen, A., & Pitkänen, T. (2015). Magnetic forces associated with bursty bulk flows in Earth's magnetotail. *Geophysical Research Letters*, **42**, 3122–3128. <https://doi.org/10.1002/2015GL063999>

Kaymaz, Z., Siscoe, G. L., & Luhmann, J. G. (1992). IMF draping around the Geotail: IMP 8 observations. *Journal of Geophysical Research*, **19**, 829–832.

Kepko, L., McPherron, R., Amm, O., Apatenkov, S., Baumjohann, W., Birn, J., & Sergeev, V. (2015a). Substorm current wedge revisited. *Space Science Reviews*, **190**, 1–46. <https://doi.org/10.1007/s11214-014-0124-9>

Kepko, L., Glassmeier, K.-H., Slavin, J. A., & Sundberg, T. (2015b). Substorm current wedge at Earth and Mercury. In A. Keiling, C. M. Jackman, & P. A. Delamere (Eds.), *Magnetotails in the solar system*. Hoboken, NJ: John Wiley. <https://doi.org/10.1002/9781118842324.ch21>

Korth, H., Anderson, B. J., Gershman, D. J., Raines, J. M., Slavin, J. A., Zurbuchen, T. H., et al. (2014). Plasma distribution in Mercury's magnetosphere derived from MESSENGER magnetometer and fast imaging plasma spectrometer observations. *Journal of Geophysical Research: Space Physics*, **119**, 2917–2932. <https://doi.org/10.1002/2013JA019567>

Korth, H., Anderson, B. J., Johnson, C. L., Slavin, J. A., Raines, J. M., & Zurbuchen, T. H. (2018). Structure and configuration of Mercury's magnetosphere. In S. C. L. R. Nittler, & B. J. Anderson (Eds.), *Mercury: The view after MESSENGER* (Chapter 16, pp. 430–460). London: Cambridge Univ. Press. ISBN: 978-1107154452

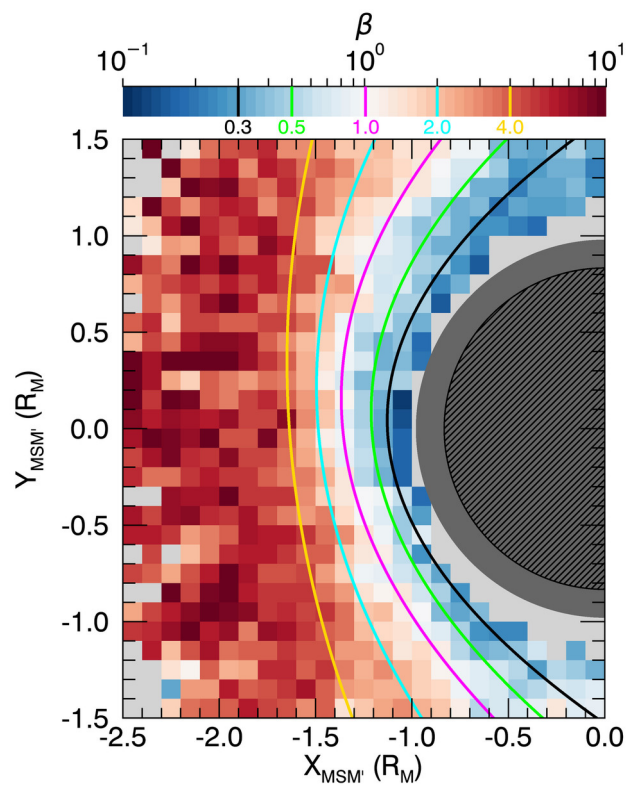
Liu, J., Angelopoulos, V., Runov, A., & Zhou, X.-Z. (2013). On the current sheets surrounding dipolarizing flux bundles in the magnetotail: The case for wedgelets. *Journal of Geophysical Research: Space Physics*, **118**, 2000–2020. <https://doi.org/10.1002/jgra.50092>

- 1240 Liu, J., Angelopoulos, V., Zhou, X.-Z., & Runov, A. (2014). Magnetic flux transport by dipolarizing
1241 flux bundles. *Journal of Geophysical Research: Space Physics*, **119**, 909–926.
1242 <https://doi.org/10.1002/2013JA019395>
1243
- 1244 McPherron, R. L., Russell, C. T., & Aubry, M. A. (1973). Satellite studies of magnetospheric substorms
1245 on August 15, 1968, 9, Phenomenological model for substorms. *Journal of Geophysical*
1246 *Research*, **78**, 3131.
1247
- 1248 Merkin, V. G., Panov, E. V., Sorathia, K., & Ukhorskiy, A. Y. (2019). Contribution of bursty bulk flows
1249 to the global dipolarization of the magnetotail during an isolated substorm. *Journal of*
1250 *Geophysical Research: Space Physics*, **124**, 8647–8668. <https://doi.org/10.1029/2019JA026872>
1251
- 1252 Nakamura, M. S., Matsumoto, H., & Fujimoto M. (2002). Interchange instability at the leading part of
1253 reconnection jets. *Geophysical Research Letters*, **29**(8), 1247.
1254 <https://doi.org/10.1029/2001GL013780>
1255
- 1256 Nakamura, R., Baumjohann, W., Mouikis, C., Kistler, L. M., Runov, A., Volwerk, M., & Balogh, A.
1257 (2004). Spatial scale of high-speed flows in the plasma sheet observed by Cluster. *Geophysical*
1258 *Research Letters*, **31**, L09804. <https://doi.org/10.1029/2004GL019558>
1259
- 1260 Ogilvie, K. W., Scudder, J. D., Vasyliunas, V. M., Hartle, R. E., & Siscoe, G. L. (1977). Observations at
1261 the planet Mercury by the plasma electron experiment, Mariner 10. *Journal of Geophysical*
1262 *Research*, **82**(13), 1807–1824. <https://doi.org/10.1029/JA082i013p01807>
1263
- 1264 Ohtani, S., Singer, H. J., & Mukai, T. (2006). Effects of the fast plasma sheet flow on the
1265 geosynchronous magnetic configuration: Geotail and GOES coordinated study. *Journal of*
1266 *Geophysical Research*, **111**, A01204. <https://doi.org/10.1029/2005JA011383>
1267
- 1268 Panov, E. V., Baumjohann, W., Nakamura, R., Kubyshkina, M. V., Glassmeier, K.-H., Angelopoulos,
1269 V., Petrukovich, A. A., & Sergeev, V. A. (2014). Period and damping factor of Pi2 pulsations
1270 during oscillatory flow braking in the magnetotail. *Journal of Geophysical Research: Space*
1271 *Physics*, **119**, 4512–4520. <https://doi.org/10.1002/2013JA019633>
1272
- 1273 Parks, G. K., Lee, E., Lin, N., Mozer, F., Wilber, M., Dandouras, I., ... Décréau, P. (2007). Solitary
1274 electromagnetic pulses detected with super-Alfvénic flows in Earth's geomagnetic tail. *Physical*
1275 *Review Letters*, **98**. <https://doi.org/10.1103/PhysRevLett.98.265001>
1276
- 1277 Poh, G., Slavin, J. A., Jia, X., Raines, J. M., Imber, S. M., Sun, W.-J., et al. (2017a). Mercury's cross-tail
1278 current sheet: Structure, X-line location and stress balance. *Geophysical Research Letters*, **44**,
1279 678–686. <https://doi.org/10.1002/2016GL071612>
1280
- 1281 Poh, G., Slavin, J. A., Jia, X., Raines, J. M., Imber, S. M., Sun, W.-J., et al. (2017b). Coupling between
1282 Mercury and its nightside magnetosphere: Cross-tail current sheet asymmetry and substorm
1283 current wedge formation. *Journal of Geophysical Research: Space Physics*, **122**, 8419–8433.
1284 <https://doi.org/10.1002/2017JA024266>
1285
- 1286 Poh, G., Slavin, J. A., Jia, X., Sun, W.-J., Raines, J. M., Imber, S. M., et al. (2018). Transport of mass
1287 and energy in Mercury's plasma sheet. *Geophysical Research Letters*, **45**, 12,163–12,170.
1288 <https://doi.org/10.1029/2018GL080601>

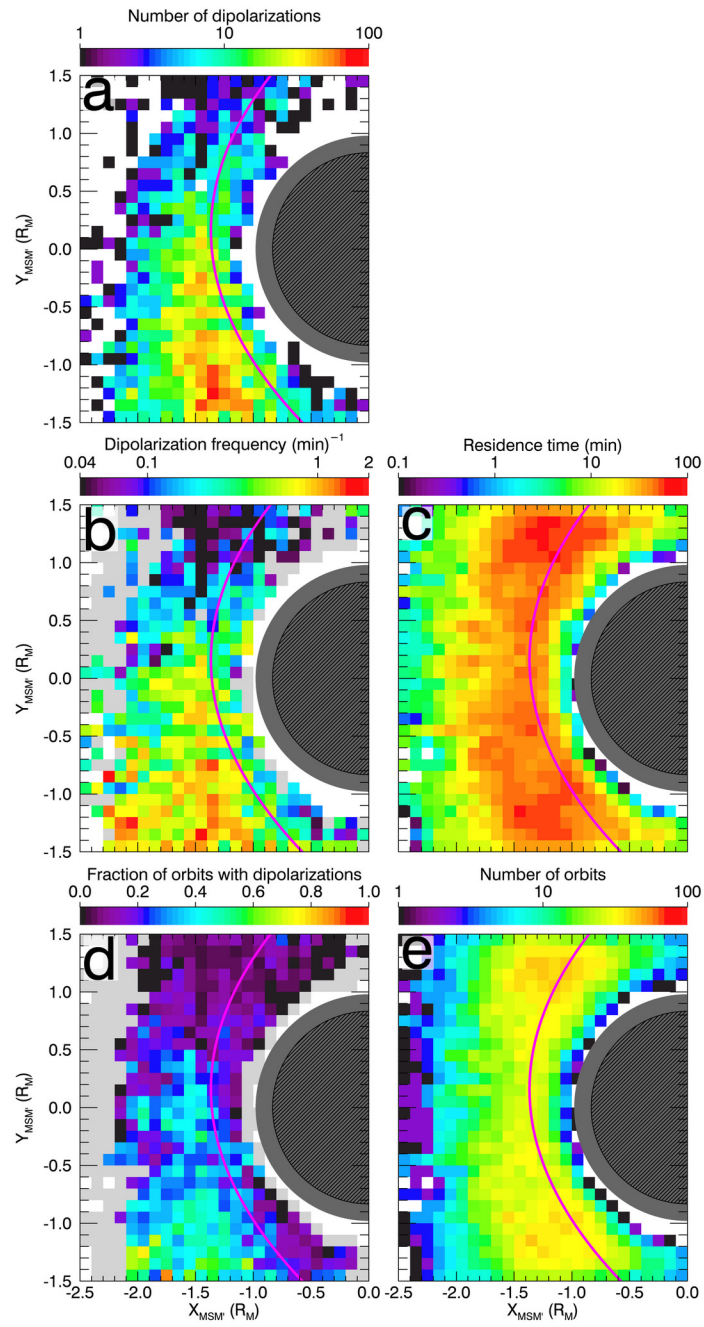
- 1289
1290 Pulkkinen, A., Rastätter, L., Kuznetsova, M., Singer, H., Balch, C., Weimer, D., et al. (2013).
1291 Community-wide validation of geospace model ground magnetic field perturbation predictions to
1292 support model transition to operations. *Space Weather*, **11**, 369–385.
1293 <https://doi.org/10.1002/swe.20056>
1294
- 1295 Raines, J. M., Slavin, J. A., Zurbuchen, T. H., Gloeckler, G., Anderson, B. J., Baker, D. N., Korth, H.,
1296 Krimigis, S. M., & McNutt Jr., R. L. (2011). MESSENGER observations of the plasma
1297 environment near Mercury. *Planetary and Space Science*, **59**(15), 2004–2015.
1298 <https://doi.org/10.1016/j.pss.2011.02.004>
1299
- 1300 Raines, J. M., Gershman, D. J., Zurbuchen, T. H., Sarantos, M., Slavin, J. A., Gilbert, J. A., et al. (2013).
1301 Distribution and compositional variations of plasma ions in Mercury's space environment: The
1302 first three Mercury years of MESSENGER observations. *Journal of Geophysical Research: Space Physics*,
1303 **118**, 1604–1619. <https://doi.org/10.1029/2012JA018073>
1304
- 1305 Raines, J. M., Gershman, D. J., Slavin, J. A., Zurbuchen, T. H., Korth, H., Anderson, B. J., ... Solomon,
1306 S. C. (2014). Structure and dynamics of Mercury's magnetospheric cusp: MESSENGER
1307 measurements of protons and planetary ions. *Journal of Geophysical Research: Space Physics*,
1308 **119**, 6587–6602. <https://doi.org/10.1002/2014JA020120>
1309
- 1310 Raines, J. M., Slavin, J. A., Tracy, P., Gershman, D. J., Zurbuchen, T., Dewey, R. M., & Sarantos, M.
1311 (2016). Plasma precipitation on Mercury's nightside and its implications for magnetospheric
1312 convection and exosphere generation. *AGU Fall Meeting 2016*, paper #SM53B-08, San
1313 Francisco, CA.
1314
- 1315 Rong, Z. J., Ding, Y., Slavin, J. A., Zhong, J., Poh, G., Sun, W. J., ... Shen, C. (2018). The magnetic
1316 field structure of Mercury's magnetotail. *Journal of Geophysical Research: Space Physics*, **123**,
1317 548–566. <https://doi.org/10.1002/2017JA024923>
1318
- 1319 Runov, A., Angelopoulos, V., Sitnov, M. I., Sergeev, V. A., Bonnell, J., McFadden, J. P., ... Auster, U.
1320 (2009). THEMIS observations of an earthward-propagating dipolarization front. *Geophysical*
1321 *Research Letters*, **36**, L14106. <https://doi.org/10.1029/2009GL038980>
1322
- 1323 Runov, A., Angelopoulos, V., & Zhou, X.-Z. (2012). Multipoint observations of dipolarization front
1324 formation by magnetotail reconnection. *Journal of Geophysical Research*, **117**, A05230.
1325 <https://doi.org/10.1029/2011JA017361>
1326
- 1327 Runov, A., Angelopoulos, V., Gabrielse, C., Zhou, X.-Z., Turner, D., & Plaschke, F. (2013). Electron
1328 fluxes and pitch-angle distributions at dipolarization fronts: THEMIS multipoint observations.
1329 *Journal of Geophysical Research: Space Physics*, **118**, 744–755.
1330 <https://doi.org/10.1002/jgra.50121>
1331
- 1332 Runov, A., Angelopoulos, V., Gabrielse, C., Liu, J., Turner, D. L., & Zhou, X.-Z. (2015). Average
1333 thermodynamic and spectral properties of plasma in and around dipolarizing flux bundles.
1334 *Journal of Geophysical Research: Space Physics*, **120**, 4369–4383.
1335 <https://doi.org/10.1002/2015JA021166>
1336
- 1337 Sergeev, V. A., Angelopoulos, V., Gosling, J. T., Cattell, C. A., & Russell, C. T. (1996). Detection of

- 1338 localized, plasma-depleted flux tubes or bubbles in the midtail plasma sheet. *Journal of*
1339 *Geophysical Research*, **101**, 10,817–10,826. <https://doi.org/10.1029/96JA00460>
1340
- 1341 Shiokawa, K., Baumjohann, W., & Haerendel, G. (1997). Braking of high-speed flows in the near-Earth
1342 tail. *Geophysical Research Letters*, **24**, 1179–1182. <https://doi.org/10.1029/97GL01062>
1343
- 1344 Shue, J.-H., Song, P., Russell, C. T., Steinberg, J. T., Chao, J. K., Zastenker, G.,...Kawano, H. (1998).
1345 Magnetopause location under extreme solar wind conditions. *Journal of Geophysical Research*,
1346 *103*, 17,691–17,700. <https://doi.org/10.1029/98JA01103>
1347
- 1348 Sitnov, M. I., Swisdak, M., & Divin, A. V. (2009). Dipolarization fronts as a signature of transient
1349 reconnection in the magnetotail. *Journal of Geophysical Research*, **114**, A04202.
1350 <https://doi.org/10.1029/2008JA013980>
1351
- 1352 Slavin, J. A., & Holzer R. E. (1981). Solar wind flow about the terrestrial planets, 1. Modeling bow
1353 shock position and shape. *Journal of Geophysical Research*, **86**, 11,401–11,418.
1354 [doi:10.1029/JA086iA13p11401](https://doi.org/10.1029/JA086iA13p11401).
1355
- 1356 Slavin, J. A., Acuna, M. H., Anderson, B. J., Baker, D. N., Benna, M., Boardsen, S. A., et al. (2009).
1357 MESSENGER observations of magnetic reconnection in Mercury's magnetosphere. *Science*,
1358 **324**(5927), 606–610. <https://doi.org/10.1126/science.1172011>
1359
- 1360 Slavin, J. A., Anderson, B. J., Baker, D. N., Benna, M., Boardsen, S. A., Gloeckler, G., ... Zurbuchen,
1361 T. H. (2010). MESSENGER observations of extreme loading and unloading of Mercury's
1362 magnetic tail. *Science*, **329**(5992), 665–668. <https://doi.org/10.1126/science.1188067>
1363
- 1364 Slavin, J. A., Anderson, B. J., Baker, D. N., Benna, M., Boardsen, S. A., Gold, R. E., et al. (2012).
1365 MESSENGER and Mariner 10 flyby observations of magnetotail structure and dynamics at
1366 Mercury. *Journal of Geophysical Research*, **117**, A01215.
1367 <https://doi.org/10.1029/2011JA016900>
1368
- 1369 Slavin, J. A., DiBraccio, G. A., Gershman, D. J., Imber, S., Poh, G. K., Raines, J., et al. (2014).
1370 MESSENGER observations of Mercury's dayside magnetosphere under extreme solar wind
1371 conditions. *Journal of Geophysical Research: Space Physics*, **119**, 8087–8116.
1372 <https://doi.org/10.1002/2014JA020319>
1373
- 1374 Slavin, J. A., Baker, D. N., Gershman, D. J., Ho, G., Imber, S. M., Krimigis, S. M., & Sundberg, T.
1375 (2018). Mercury's dynamic magnetosphere. In S. C. L. R. Nittler, & B. J. Anderson (Eds.),
1376 *Mercury: The view after MESSENGER* (Chapter 17, pp. 461–496). London: Cambridge Univ.
1377 Press. ISBN: 978-1107154452
1378
- 1379 Smith, A.W., Slavin, J. A., Jackman, C.M., Poh, G.-K., & Fear, R. C. (2017). Flux ropes in the Hermean
1380 magnetotail: Distribution, properties, and formation. *Journal of Geophysical Research: Space*
1381 *Physics*, **122**, 8136–8153. <https://doi.org/10.1002/2017JA024295>
1382
- 1383 Sun, W. J., Fu S. Y., Parks, G. K., Liu, J., Yao, Z. H., Shi, Q. Q., Zong, Q. G., Huang, S. Y., Pu, Z. Y.,
1384 & Xiao, T. (2013). Field-aligned currents associated with dipolarizations fronts. *Geophysical*
1385 *Research Letters*, **40**(17), 4503–4508. <https://doi.org/10.1002/grl.50902>
1386

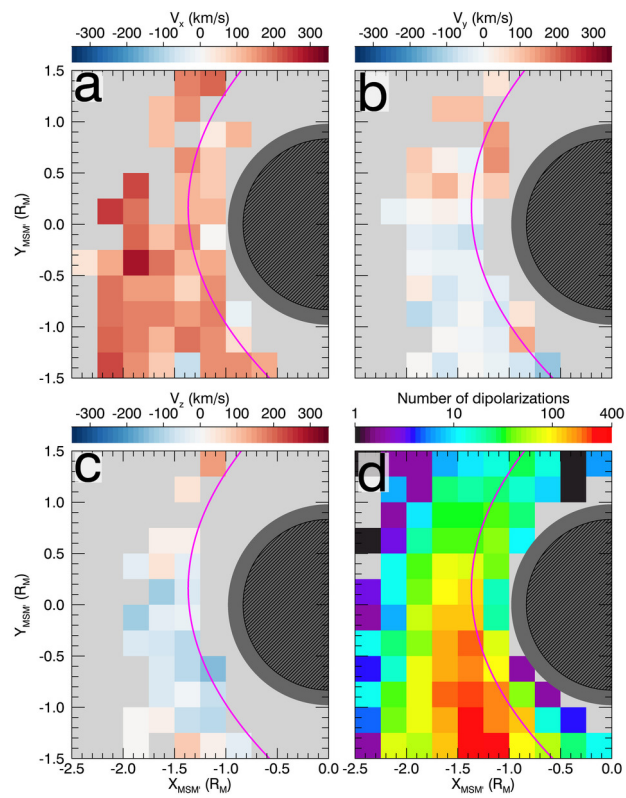
- 1387 Sun, W.-J., Slavin, J. A., Fu, S., Raines, J. M., Sundberg, T., Zong, Q. G., et al. (2015). MESSENGER
1388 observations of Alfvénic and compressional waves during Mercury’s substorms. *Geophysical*
1389 *Research Letters*, **42**, 6189–6198. <https://doi.org/10.1002/2015GL065452>
1390
- 1391 Sun, W. J., Fu, S. Y., Slavin, J. A., Raines, J. M., Zong, Q. G., Poh, G. K., & Zurbuchen, T. H. (2016).
1392 Spatial distribution of Mercury’s flux ropes and reconnection fronts: MESSENGER
1393 observations. *Journal of Geophysical Research: Space Physics*, **121**, 7590–7607.
1394 <https://doi.org/10.1002/2016JA022787>
1395
- 1396 Sun, W. J., Raines, J. M., Fu, S. Y., Slavin, J. A., Wei, Y., Poh, G. K., et al. (2017). MESSENGER
1397 observations of the energization and heating of protons in the near-Mercury magnetotail.
1398 *Geophysical Research Letters*, **44**, 8149–8158. <https://doi.org/10.1002/2017GL074276>
1399
- 1400 Sun, W. J., Slavin, J. A., Dewey, R. M., Raines, J. M., Fu, S. Y., Wei, Y., et al. (2018). A comparative
1401 study of the proton properties of magnetospheric substorms at Earth and Mercury in the near
1402 magnetotail. *Geophysical Research Letters*, **45**, 7933–7941.
1403 <https://doi.org/10.1029/2018GL079181>
1404
- 1405 Sun, W. J., Slavin, J. A., Dewey, R. M., Chen, Y., DiBraccio, G. A., Raines, J. M., Jasinski, J. M., Jia,
1406 X., Akhavan-Tafti, M. (2020). MESSENGER observations of Mercury’s nightside
1407 magnetosphere under extreme solar wind conditions: reconnection-generated structures and
1408 steady convection. *Journal of Geophysical Research: Space Physics*.
1409 <https://doi.org/10.1029/2019JA027490>
1410
- 1411 Sundberg, T., Slavin, J. A., Boardsen, S. A., Anderson, B. J., Korth, H., Ho, G. C., et al. (2012).
1412 MESSENGER observations of dipolarization events in Mercury’s magnetotail. *Journal of*
1413 *Geophysical Research*, **117**, A00M03. <https://doi.org/10.1029/2012JA017756>
1414
- 1415 Ukhorskiy, A. Y., Sorathia, K. A., Merkin, V. G., Sitnov, M. I., Mitchell, D. G., & Gkioulidou, M.
1416 (2018). Ion trapping and acceleration at dipolarization fronts: High-resolution MHD and test-
1417 particle simulations. *Journal of Geophysical Research: Space Physics*, **123**, 5580–5589.
1418 <https://doi.org/10.1029/2018JA025370>
1419
- 1420 Winslow, R. M., Anderson, B. J., Johnson, C. L., Slavin, J. A., Korth, H., Purucker, M. E., ... Solomon,
1421 S. C. (2013). Mercury’s magnetopause and bow shock from MESSENGER Magnetometer
1422 observations. *Journal of Geophysical Research: Space Physics*, **118**, 2213–2227.
1423 <https://doi.org/10.1002/jgra.50237>
1424
- 1425 Zhong, J., Wan, W. X., Wei, Y., Slavin, J. A., Raines, J. M., Rong, Z. J., Chari, L. H., & Han, X. H.
1426 (2015). Compressibility of Mercury’s dayside magnetosphere. *Geophysical Research Letters*, **42**,
1427 10135–10139. <https://doi.org/10.1002/2015GL067063>



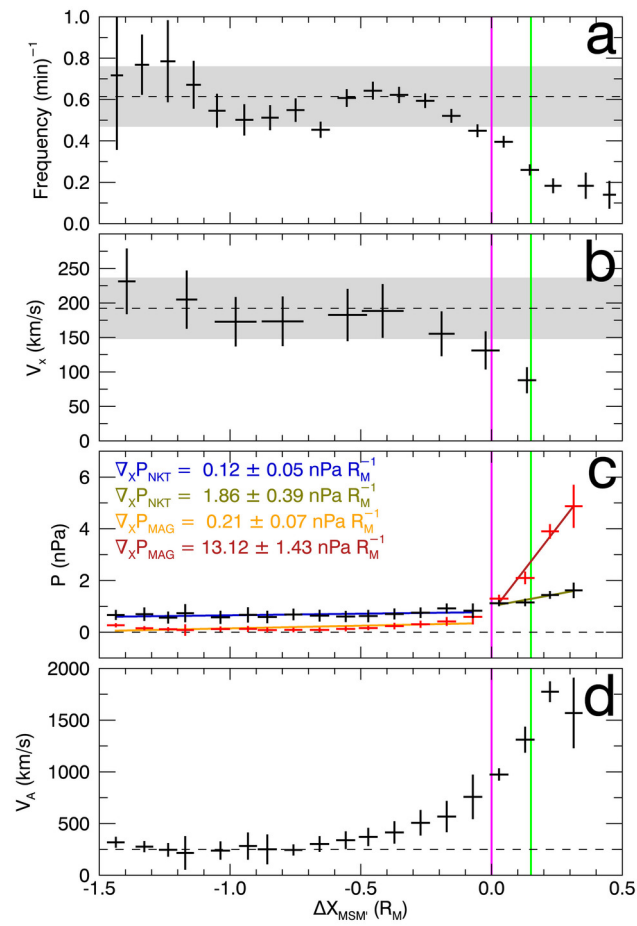
JGRA_55966_2020JA028112-f01-z-jpg



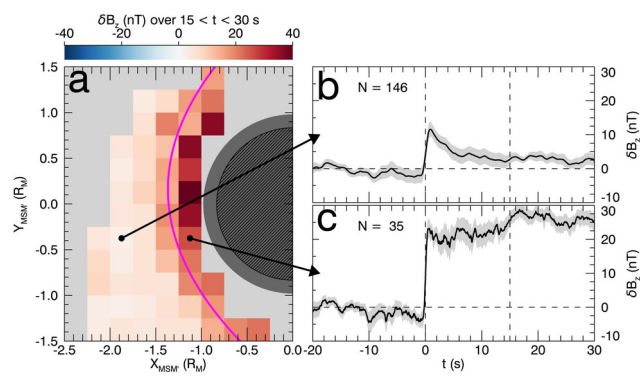
JGRA_55966_2020JA028112-f02-z-.jpg



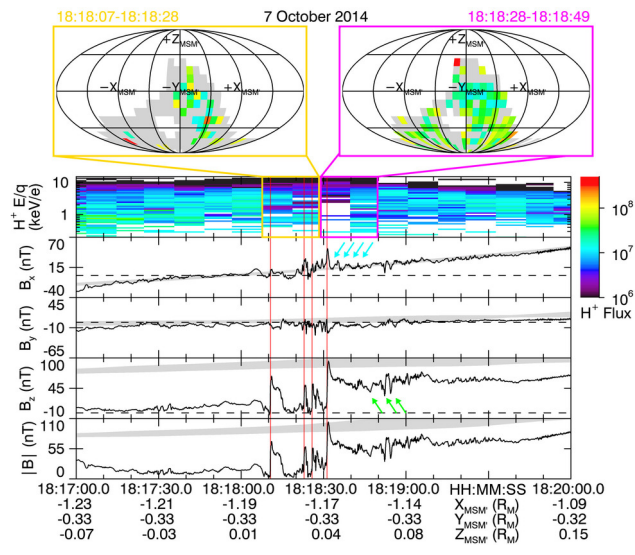
JGRA_55966_2020JA028112-f03-z-jpg



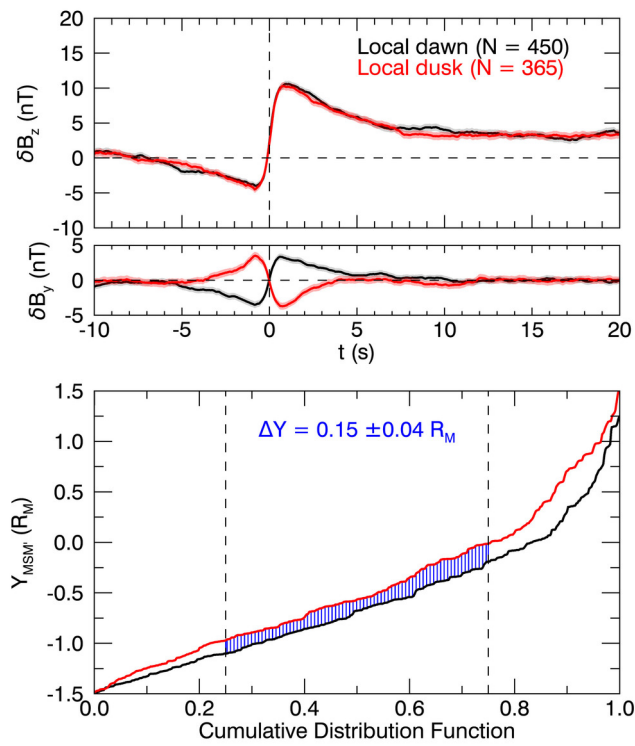
JGRA_55966_2020JA028112-f04-z-jpg



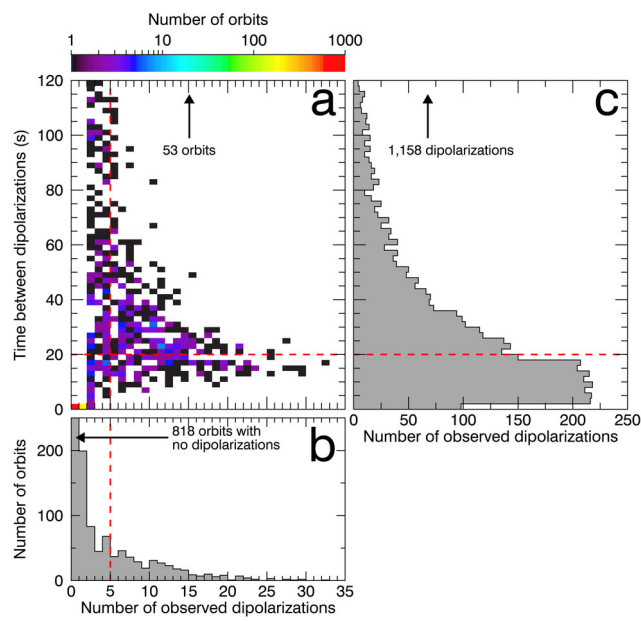
JGRA_55966_2020JA028112-f05-z-.jpg



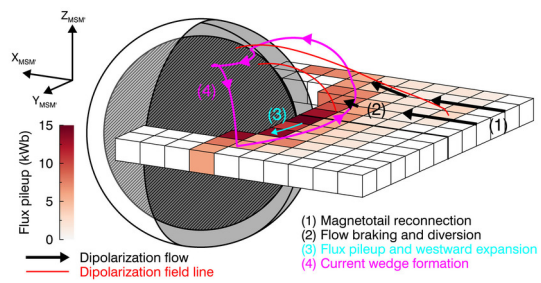
JGRA_55966_2020JA028112-f06-z-jpg



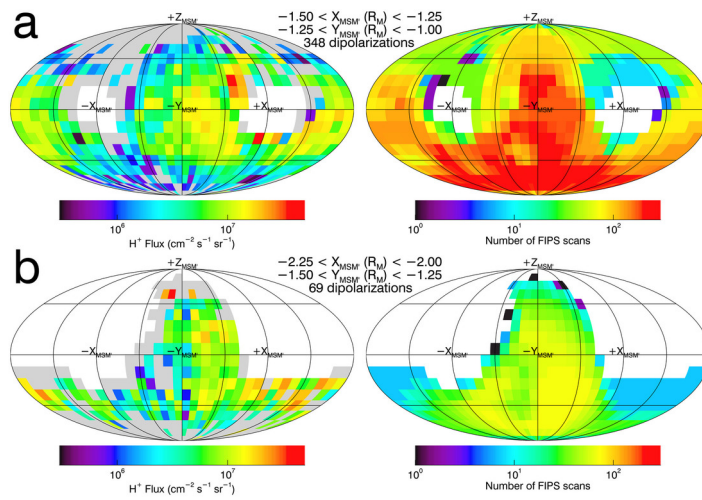
JGRA_55966_2020JA028112-f07-z-.jpg



JGRA_55966_2020JA028112-f08-z-.jpg



JGRA_55966_2020JA028112-f09-z-.jpg



JGRA_55966_2020JA028112-f10-z-jpg